RESOURCE
https://doi.org/10.1038/s41556-020-0488-x

nature cell biology

Check for updates

Systems analysis of RhoGEF and RhoGAP regulatory proteins reveals spatially organized RAC1 signalling from integrin adhesions

Paul M. Müller[1,10], Juliane Rademacher[1,10], Richard D. Bagshaw[2,10], Celina Wortmann[1], Carolin Barth[1], Jakobus van Unen[3], Keziban M. Alp[1], Girolamo Giudice[4], Rebecca L. Eccles[1], Louise E. Heinrich[5], Patricia Pascual-Vargas[5], Marta Sanchez-Castro[2], Lennart Brandenburg[1], Geraldine Mbamalu[2], Monika Tucholska[2], Lisa Spatt[1], Maciej T. Czajkowski[1,6], Robert-William Welke[1], Sunqu Zhang[2], Vivian Nguyen[2], Trendelina Rrustemi[1], Philipp Trnka[1], Kiara Freitag[1], Brett Larsen[2], Oliver Popp[1,6], Philipp Mertins[1,6], Anne-Claude Gingras[2,7], Frederick P. Roth[2,8,9], Karen Colwill[2], Chris Bakal[5], Olivier Pertz[3], Tony Pawson[2,7,11], Evangelia Petsalaki[2,4] ✉ and Oliver Rocks[1,2] ✉

Rho GTPases are central regulators of the cytoskeleton and, in humans, are controlled by 145 multidomain guanine nucleotide exchange factors (RhoGEFs) and GTPase-activating proteins (RhoGAPs). How Rho signalling patterns are established in dynamic cell spaces to control cellular morphogenesis is unclear. Through a family-wide characterization of substrate specificities, interactomes and localization, we reveal at the systems level how RhoGEFs and RhoGAPs contextualize and spatiotemporally control Rho signalling. These proteins are widely autoinhibited to allow local regulation, form complexes to jointly coordinate their networks and provide positional information for signalling. RhoGAPs are more promiscuous than RhoGEFs to confine Rho activity gradients. Our resource enabled us to uncover a multi-RhoGEF complex downstream of G-protein-coupled receptors controlling CDC42–RHOA crosstalk. Moreover, we show that integrin adhesions spatially segregate GEFs and GAPs to shape RAC1 activity zones in response to mechanical cues. This mechanism controls the protrusion and contraction dynamics fundamental to cell motility. Our systems analysis of Rho regulators is key to revealing emergent organization principles of Rho signalling.

Rho GTPases coordinate changes in cytoskeletal architecture to drive fundamental cell behaviours in all eukaryotes[1,2]. Defects in Rho signalling have been linked to cancer metastasis and other diseases[3]. Rho proteins typically cycle between an inactive GDP-bound form and an active GTP-bound form[4]. Following activation, they bind effector proteins to elicit cytoskeletal remodelling. Their activity cycle is initiated by guanine nucleotide exchange factors (RhoGEFs)[5,6] and terminated by GTPase-activating proteins (RhoGAPs)[7]. In addition, guanine nucleotide dissociation inhibitors (RhoGDIs) sequester and inactivate the GTPases in the cytosol[8,9]. This coupling of the GDP/GTP cycle to a membrane association–dissociation cycle adds another layer of regulation. With 145 members, the RhoGEF and RhoGAP multidomain proteins vastly outnumber the 10 classical Rho family GTPase switch proteins that they regulate[10], which enables intricate control of Rho signalling specificity (Extended Data Fig. 1).

Rho signalling responses in cells are highly localized[11] and have been observed in distinct subcellular zones[12–16], with several GTPases operating simultaneously. Cell morphogenesis therefore involves the concerted action of multiple Rho family members and their regulators, which together form complex networks[17,18]. However, our understanding of how the Rho signalling system coordinates such specific and spatially confined cell responses is limited and stems from studies of individual Rho regulators, while a systems-level view is lacking.

Here, we present a family-wide characterization of RhoGEFs and RhoGAPs regarding their substrate specificities for the prototype GTPases RHOA, RAC1 and CDC42, their interactomes and their subcellular localization. It places the regulators into their functional context and provides a framework for future targeted studies of their diverse roles in controlling Rho GTPases. Our study uncovers systems-level behaviour of the RhoGEFs and RhoGAPs, showing how they collectively shape and contextualize Rho activity gradients. The data reveal how, in response to mechanical cues, GEFs and GAPs are segregated on integrin adhesions to control spatially distributed morphodynamic responses driving cell migration.

Results

To characterize the mammalian RhoGEFs and RhoGAPs, we generated an expression library comprising 141 full-length complementary DNAs (64 Dbl family GEFs, 11 Dock family GEFs, 64 GAPs and 2 dual GEFs/GAPs), almost all of which represent the longest isoform known to exist (Extended Data Fig. 1; Supplementary Table 1).

[1]Max-Delbrück-Center for Molecular Medicine, Berlin, Germany. [2]Lunenfeld-Tanenbaum Research Institute, Sinai Health System, Toronto, Ontario, Canada. [3]Institute of Cell Biology, University of Bern, Bern, Switzerland. [4]European Molecular Biology Laboratory, European Bioinformatics Institute, Wellcome Genome Campus, Hinxton, UK. [5]Institute of Cancer Research, Chester Beatty Laboratories, London, UK. [6]Berlin Institute of Health (BIH), Berlin, Germany. [7]Department of Molecular Genetics, University of Toronto, Toronto, Ontario, Canada. [8]Donnelly Centre and Departments of Molecular Genetics and Computer Science, University of Toronto, Toronto, Ontario, Canada. [9]Canadian Institute for Advanced Research, Toronto, Ontario, Canada. [10]These authors contributed equally: Paul M. Müller, Juliane Rademacher, Richard D. Bagshaw. [11]Deceased: Tony Pawson. ✉e-mail: petsalaki@ebi.ac.uk; oliver.rocks@mdc-berlin.de

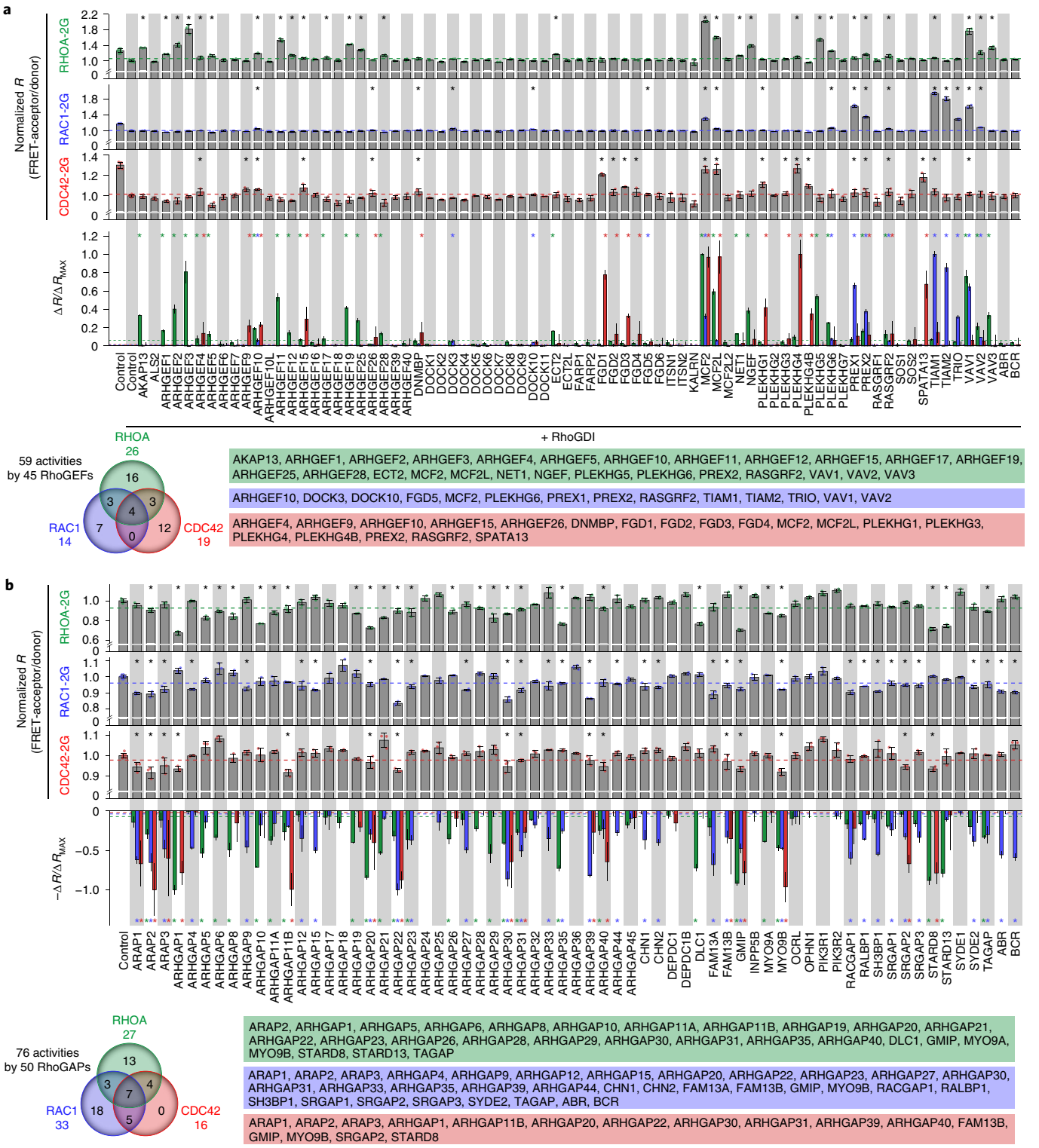

Fig. 1 | Family-wide RhoGEF and RhoGAP activity screens. a, FRET-based RhoGEF activity assay: HEK293T cells were transfected with the mCherry-labelled RhoGEF cDNA library and the FRET sensors RHOA-2G, RAC1-2G or CDC42-2G together with RhoGDI (where indicated). **b**, FRET-based RhoGAP activity assay: RhoGDI shRNA-depleted HEK293T cells were transfected with the mCherry-labelled RhoGAP cDNA library and the indicated sensors. FRET ratio (*R*) values were normalized to control+RhoGDI (**a**) or control (**b**) and are shown as the mean ± s.d. ($n = 3$ independent experiments). Broken lines indicate activity thresholds. The significance of values above (**a**) or below (**b**) the threshold was calculated using unpaired two-sided Student's *t*-tests versus control+RhoGDI (**a**) or control (**b**) and the Benjamini–Hochberg procedure; significant values are marked by asterisks. Graphs below show quantification of RhoGEF and RhoGAP activities towards RHOA (green), RAC1 (blue) and CDC42 (red), allowing direct comparison. Changes in FRET ratio (ΔR) values compared with control+RhoGDI (**a**) or control (**b**) were normalized to the maximal observed FRET ratio change (ΔR_{MAX}) in each assay. For regulators with multiple activities, only those above 20% of the main substrate activity were considered (marked by asterisks). Venn diagrams and lists of regulators with activity are displayed sorted by the substrate GTPases RHOA, RAC1 and CDC42. Source data including *P* values are provided in Source Data Fig. 1.

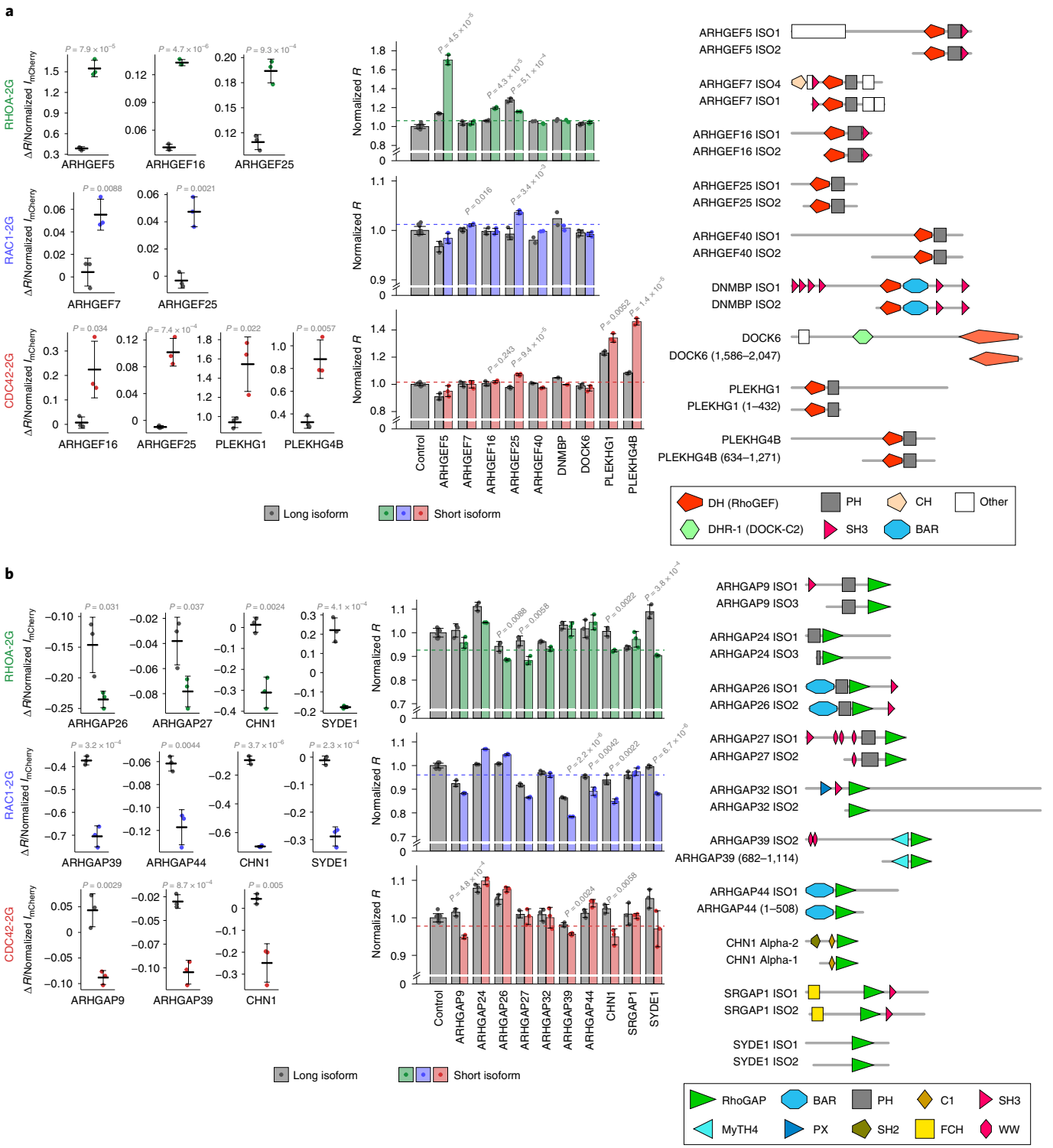

Fig. 2 | Autoinhibition is a common feature of RhoGEFs and RhoGAPs. a,**b**, Semiquantitative comparison of catalytic activities of full-length longest isoforms versus shorter isoforms or truncations of randomly selected nine RhoGEFs (**a**) and ten RhoGAPs (**b**). Experiments were performed as described in Fig. 1. Left: the graphs show the mean change in FRET ratio (ΔR) normalized to RhoGEF or RhoGAP expression levels as determined by normalized mCherry intensity (normalized $I_{mCherry}$) (horizontal black line) ± s.d. ($n = 3$ independent experiments). Middle: graphs show the mean FRET ratio (R) values normalized to control ± s.d. ($n = 3$ independent experiments; results from two independent experiments are shown for ARHGEF40 and DNMBP). Broken lines indicate activity thresholds, as in Fig. 1. Statistical significance was calculated using unpaired two-sided Student's t-tests. Right: domain representations of the constructs used, as shown in Extended Data Fig. 1. ISO, isoform. Source data are provided in Source Data Fig. 2.

Not included are OBSCN (~8,000 amino acids) and ARHGEF33, ARHGEF37 and ARHGEF38, which were originally not predicted as RhoGEFs.

Family-wide activity screen reveals that RhoGAPs are more promiscuous than RhoGEFs. First, we systematically characterized the substrate specificities of all regulators to link them to their cognate

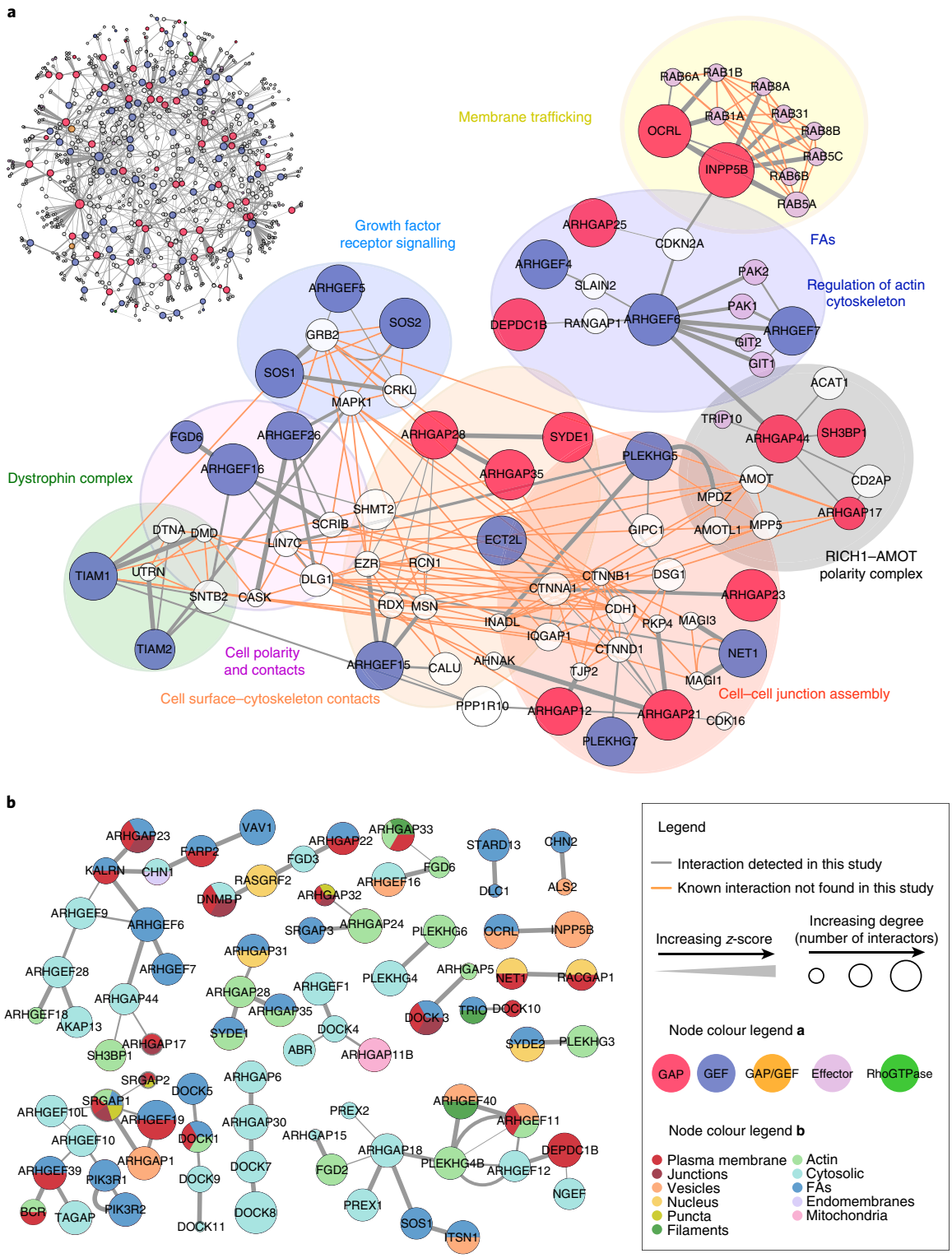

Fig. 3 | The RhoGEF and RhoGAP interactome is highly interconnected and includes components of multiple cellular processes. a, The RhoGEF and RhoGAP interactome network. As examples of subnetworks of the RhoGEF and RhoGAP interactome, interactions with complexes involved in cell polarity, junctions, membrane trafficking, growth factor receptor signalling and actin cytoskeleton organization are shown. The orange lines indicate interactions among the prey of the tested regulators. **b**, Enrichment of interactions among RhoGEFs and RhoGAPs ($n = 1,292$ interactions, two-sided Fisher's exact test, $P < 0.001$). Shown are all 66 bait–bait interactions, with nodes colour-coded by their subcellular localization (see also Fig. 5d).

Rho GTPase downstream pathways. An extensive literature curation of claimed specificities revealed an incomplete data landscape with a high degree of conflict among reports (Supplementary Table 2). We therefore developed a screening-compatible live-cell imaging assay, using fluorescence resonance energy transfer (FRET)-based biosensors for the prototype GTPases RAC1, CDC42 and RHOA[15,19,20] (Extended Data Fig. 2; Supplementary Information). This approach enabled the analysis of ectopically expressed full-length regulators

in their native cellular environment. We found catalytic activities for 45 out of 75 RhoGEFs and 48 out of 63 RhoGAPs. In addition, the dual GEFs/GAPs ABR and BCR exhibited GAP activity (Fig. 1; Supplementary Table 2). The positive hits included regulators with high substrate specificity (35 RhoGEFs, 31 RhoGAPs) and many that regulate multiple Rho GTPases (10 RhoGEFs, 19 RhoGAPs). Our data therefore not only reveal extensive promiscuity among regulators but also that the inactivating RhoGAPs are less selective than the activating RhoGEFs ($P=0.02$; Supplementary Table 2). This agrees with our literature survey showing twofold higher promiscuity for RhoGAPs compared with RhoGEFs (21 out of 49 active GAPs versus 15 out of 65 active GEFs; see the 'reference list' in Supplementary Table 2). Promiscuity has been predominantly reported for the co-regulation of CDC42 and RAC1 (refs. [1,21]). However, we found a similar number of regulators that control RHOA together with CDC42 and/or RAC1 (16 versus 18 and 17).

While our data largely agreed with existing data (70%; see the reference list in Supplementary Table 2), we describe ten previously unidentified activities. PLEKHG4B, for instance, is a strong exclusive CDC42 GEF (see also Fig. 4), and SYDE2 is a RAC1-specific GAP. The screen also revealed discrepancies with the literature. The previously proposed representative CDC42-specific GAPs ARHGAP1, ARHGAP17 and ARHGAP31 showed either no activity towards this GTPase or more efficiently inactivated RAC1 in our assay. In fact, none of the GAPs tested exhibited exclusive substrate specificity for CDC42, although 21 GAPs promiscuously regulated CDC42. By contrast, we found exclusive CDC42 activity for a total of 12 GEFs. Overall, we provide a standardized, systematic analysis of RhoGEF and RhoGAP substrate specificities in cells as a reference for future studies.

Autoinhibition is a common feature of RhoGEFs and RhoGAPs. Some RhoGEFs and RhoGAPs displayed minimal or no activity in our screen. A requirement for release from autoinhibition via mechanisms such as phosphorylation, protein or lipid interactions may account for the observed lack of activity[22]. To study whether autoinhibition is a general mechanism in controlling the Rho regulators, we included shorter forms of nine RhoGEFs and ten RhoGAPs, which lack potential regulatory elements that are present in the longest isoforms. Thirteen of these exhibited a higher catalytic efficiency than their longer counterparts (Fig. 2). This shows that cellular regulatory conditions are preserved in our assay and could explain why activities of strongly autoinhibited regulators have not been detected. The longest isoform of ARHGAP9 only exhibited catalytic activity towards RAC1. Surprisingly, isoform 3, which lacks an amino-terminal SH3 domain, also inactivated CDC42, which suggests that autoregulatory features might also affect the substrate selectivity of Rho regulators. Our data show that RhoGEFs and RhoGAPs are widely autoinhibited and suggest that they respond to local cues and feedback regulation.

Interactome analysis reveals that many RhoGEFs and RhoGAPs associate with each other in complexes. Next, we used affinity purification coupled to mass spectrometry (MS) to obtain a high-quality RhoGEF and RhoGAP network of 1,292 interactions (1,082 of which were novel) among 863 proteins (Fig. 3a; Supplementary Table 3, 'silver set'). This interactome explores a largely uncharted part of the human interactome and connects the Rho regulatory system to functional complexes that link the actin cytoskeleton to critical cell functions (Fig. 3a; Extended Data Fig. 3a,b). Our dataset therefore provides a rich source of information that can be used for targeted studies to further dissect the interplay of Rho GTPases with other signalling pathways[23].

Notably, in addition to 20 interactions with Rho effector proteins and 24 interactions with small GTPases, our network includes 66 interactions among RhoGEFs and RhoGAPs themselves (Fig. 3b). In support of their functional relevance, we found that these pairs of interacting regulators are co-expressed (Methods; $P=7\times10^{-5}$, Wilcoxon test). Moreover, we validated 22 out of 26 randomly selected RhoGEF and RhoGAP interactions by co-immunoprecipitation (Extended Data Fig. 4; Supplementary Information). Both homotypic and heterotypic interactions occurred, with fewer complexes between RhoGAPs (24 GEF/GAP, 28 GEF/GEF, 11 GAP/GAP and 3 GEF-ABR or GEF-BCR). Our data indicate a previously unrecognized extensive interplay between Rho regulators to jointly coordinate Rho signalling networks.

A multi-RhoGEF complex downstream of GPCR signalling mediates RHOA–CDC42 crosstalk. As a case study, we functionally characterized a multi-RhoGEF complex identified in our network: the interaction between the as yet undescribed PLEKHG4B with ARHGEF11 (also known as PDZ-RhoGEF) and ARHGEF12 (also known as LARG). ARHGEF11 and ARHGEF12 are two well-studied activators of RHOA signalling downstream of G-protein-coupled receptors (GPCRs) and have essential roles in chemokine-driven tumour cell invasion[24,25] (Figs. 3b and 4). ARHGEF11 and ARHGEF12 are engaged following GPCR stimulation by binding to activated heterotrimeric $G\alpha_{12}$ and $G\alpha_{13}$

Fig. 4 | A multi-RhoGEF complex downstream of GPCRs mediates RHOA–CDC42 crosstalk. a, Schematics of the three human RhoGEFs and truncations used in this study. **b**, ARHGEF11 and ARHGEF12 specifically interact with PLEKHG4B. Representative immunoprecipitations (IPs) of all eight PLEKHG family proteins (GFP) with FLAG-tagged ARHGEF11 or ARHGEF12 (GEF11/12) from HEK293T cell lysates. Data shown represent two and three independent experiments for ARHGEF11 and ARHGEF12, respectively. **c**, ARHGEF11 (GEF11) and ARHGEF12 (GEF12) are RHOA-specific GEFs, whereas PLEKHG4B (4B) activates CDC42. FRET assay and statistics are as described in Fig. 1a. ARHGEF11-Y885A (GEF11-Y885A), ARHGEF12-Y940A (GEF12-Y940A) and PLEKHG4B-Y943A (4B-Y93A) are GEF-dead mutants. **d**, Sequence alignment of the three human GEFs revealing the conserved tyrosine residue in the DH domain that is critical for catalysis[62]. **e**, Autoinhibition of PLEKHG4B and its release by ARHGEF11 and ARHGEF12 binding. Left: PLEKHG4B-stimulated SRE.L luciferase reporter activation assay in HEK293T cells expressing the indicated constructs. Right: CDC42-2G FRET ratios of cells transfected with RhoGDI, mCherry-tagged PLEKHG4B constructs and indicated miRFP-tagged ARHGEF11 and ARHGEF12 mutants. **f**, ARHGEF11 and ARHGEF12 are inhibited by PLEKHG4B. Upper: ARHGEF11 and ARHGEF12-stimulated SRE.L luciferase reporter activation assay. The anti-FLAG western blot shows the expression of the transfected constructs. Lower: RHOA-2G FRET ratios of cells transfected with RhoGDI, mCherry-ARHGEF11 and ARHGEF12 and the indicated miRFP-tagged PLEKHG4B mutants. **g**, PLEKHG4B inhibits $G\alpha_{13}$-mediated ARHGEF11 and ARHGEF12 recruitment. Left: representative IP of the three GEFs (GFP) with wild-type (WT) or constitutively active FLAG-$G\alpha_{13}$ (Q226L; QL). Data shown represent three independent experiments. Right: representative IP of YFP-tagged ARHGEF11 and ARHGEF12 with indicated FLAG-tagged proteins. Data shown represent two independent experiments. **h**, Model of PLEKHG4B interactions with the ARHGEF11–ARHGEF12 dimer[63] and their mutual regulation of $G\alpha_{12/13}$-mediated GPCR signalling. All bar graphs show the mean ± s.d. ($n=3$ independent experiments in **c** and **f** (upper); $n=3$ independent samples of one experiment in **e** (left), representative out of three experiments, with similar results obtained; $n=4$ independent experiments in **f** (lower)). For **c**, **e** (right) and **f**, significance was calculated using unpaired two-sided Student's *t*-tests versus control+RhoGDI (**c**), versus PLEKHG4B (**e**, right), versus FLAG (**f**, upper) or as indicated by lines. For **e** (left), significance was determined using one-way ANOVA, followed by Tukey's multiple comparisons. Significance is ranked as follows: $^{*}P<0.05$, $^{**}P<0.01$, $^{***}P<0.001$, NS, not significant. Numerical source data, including *P* values, and unprocessed blots related to **b**, **f** and **g** are provided in Source Data Fig. 4.

subunits[26]. PLEKHG4B, but not the other seven members of the PLEKHG (Pleckstrin homology domain-containing family G) proteins, interacted with these two GEFs (Fig. 4b; Extended Data Fig. 5a). While ARHGEF11 and ARHGEF12 are RHOA-specific, PLEKHG4B selectively activated CDC42 (Fig. 4c) and draws an additional Rho GTPase substrate into this multi-GEF assembly. PLEKHG4B is subject to autoinhibition, as truncation of its N terminus increased its CDC42 GEF activity (Fig. 4e; Extended Data Fig. 5b). An increase in CDC42 GEF activity of full-length PLEKHG4B was also induced when it was co-expressed either N-terminal fragments of ARHGEF11 or ARHGEF12 or catalytically inactive mutants (Fig. 4d,e). This shows that the binding of PLEKHG4B to its partner GEFs releases its autoinhibition. Conversely, coexpressing an N-terminal fragment of PLEKHG4B or its GEF-inactive mutant strongly decreased the catalytic activities of ARHGEF11 and ARHGEF12 towards RHOA (Fig. 4d,f). Moreover, in the context of GPCR signalling, both ARHGEF11 and ARHGEF12 selectively associated with constitutively active

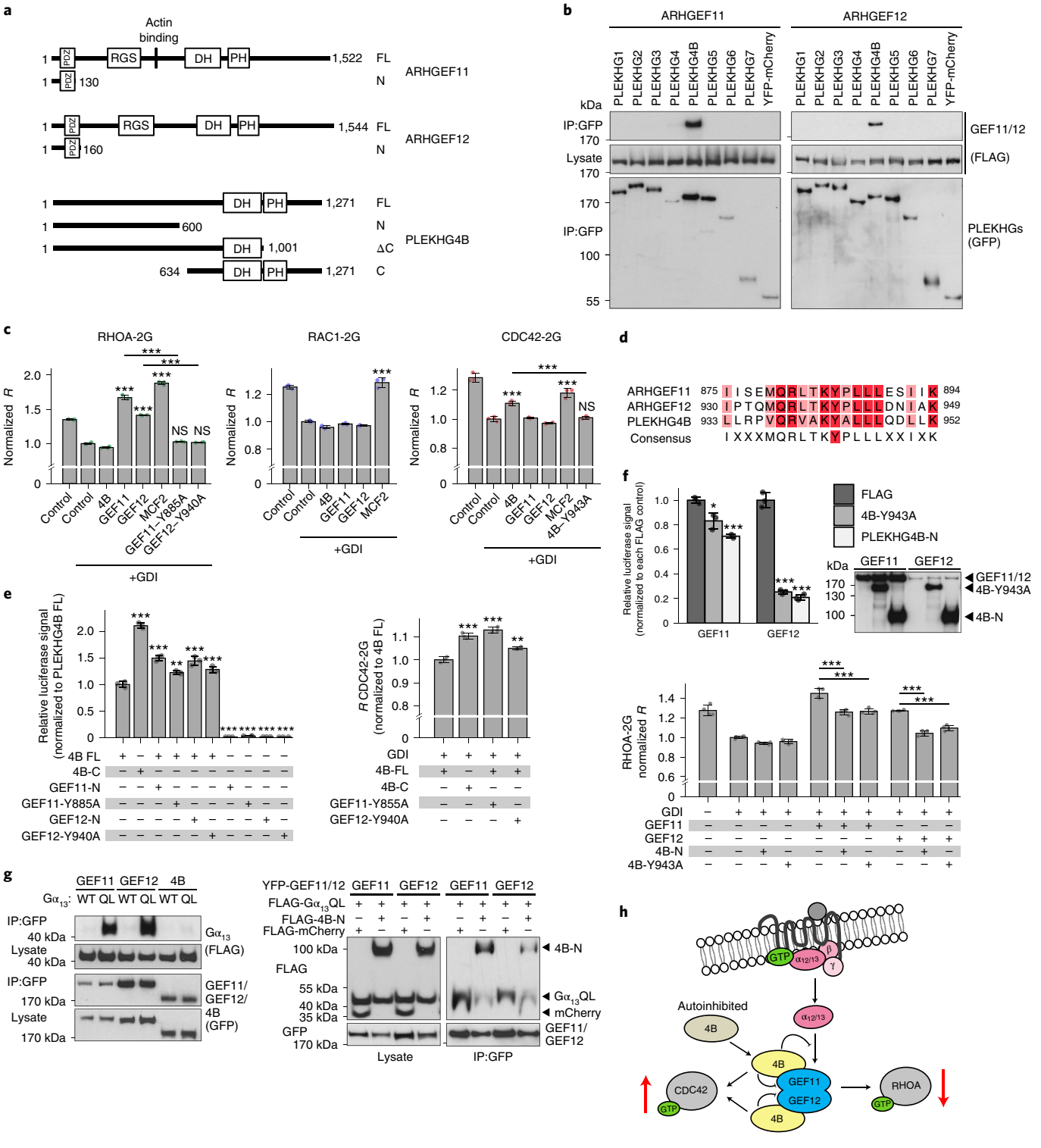

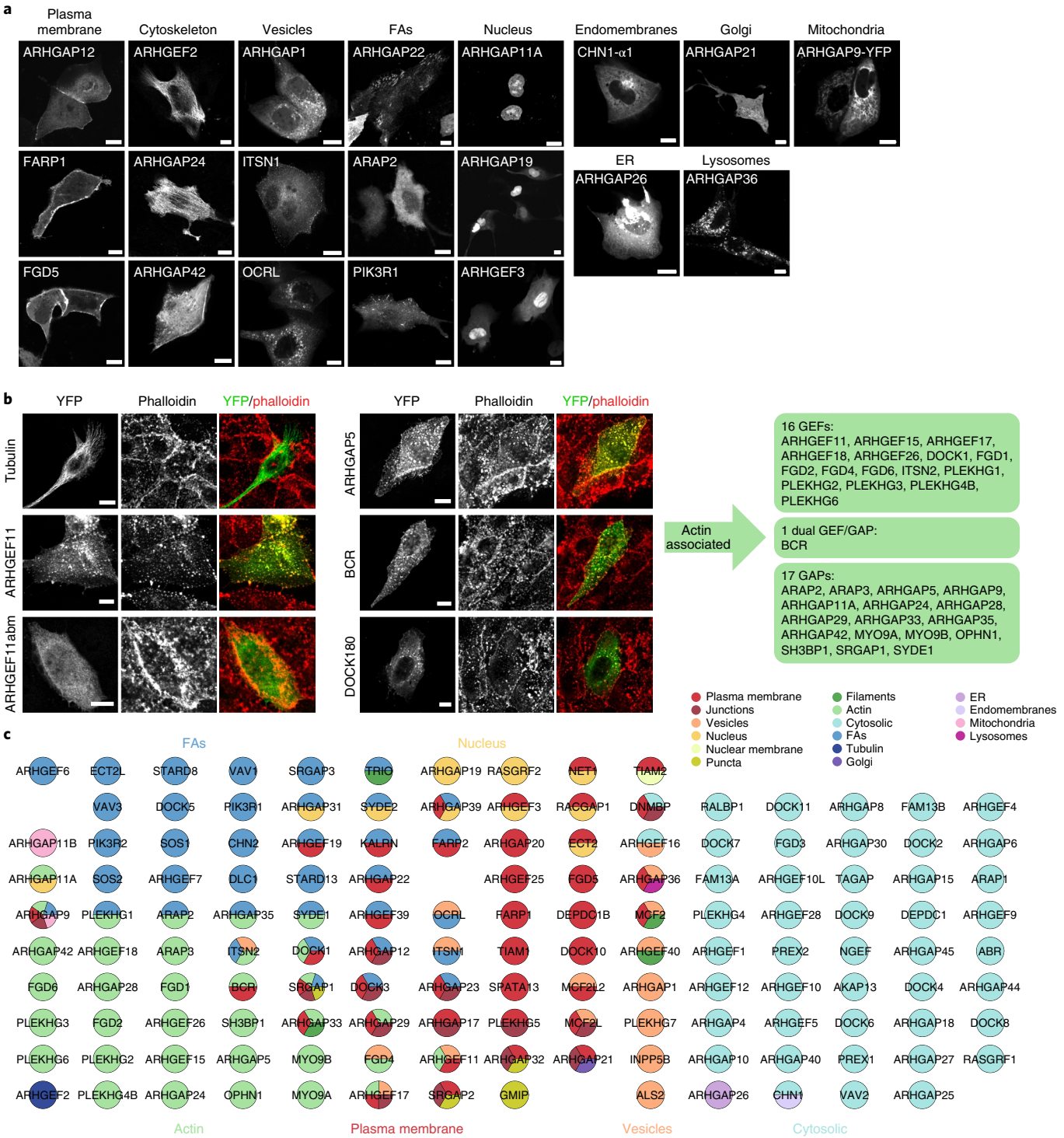

Fig. 5 | Spatial distribution of RhoGEFs and RhoGAPs. a, Selection of MDCK live-cell images from a confocal microscopy screen showing the localization of YFP-tagged RhoGEFs and RhoGAPs to different subcellular structures. See Supplementary Fig. 1 for the full dataset. **b**, Actin association assessed by confocal imaging of fixed, cytochalasin D-treated MDCK cells transiently transfected with the indicated YFP-tagged RhoGEFs, RhoGAPs or controls. abm, actin-binding mutant[64]; ER, endoplasmic reticulum. **c**, Summary of the distribution of RhoGEFs and RhoGAPs over different subcellular compartments and structures. Scale bars, 10 µm. For **a** and **b**, representative images of two independent experiments (with five images obtained for each experiment) are shown, with similar results obtained.

$G\alpha_{13}$QL, as expected. The addition of PLEKHG4B, however, inhibited this interaction (Fig. 4g, right).

The three GEFs therefore mutually control their catalytic activities. ARHGEF11 and ARHGEF12 enhance the CDC42 GEF activity of PLEKHG4B. In return, PLEKHG4B inhibits ARHGEF11 and ARHGEF12-mediated RHOA activation in the following two ways: directly by reducing their catalytic activity and indirectly by perturbing their engagement with GPCRs via $G\alpha_{12/13}$ (Fig. 4h).

Our resource enabled us to provide proof of concept of a mechanism of cross-talk among Rho GTPases in a pathway previously thought to only activate RHOA[27].

RhoGEFs and RhoGAPs provide positional information to Rho GTPase signalling regulation. To understand how RhoGEFs and RhoGAPs contribute spatial information to Rho signalling, we mapped their subcellular distribution. Confocal live-cell microscopy of yellow fluorescent protein (YFP) fusion proteins in MDCK epithelial cells revealed that over half of RhoGEFs and RhoGAPs inherently localize to one or more distinct structures at steady-state, thereby collectively decorating virtually all cellular compartments (Fig. 5a,c; Supplementary Fig. 1; Supplementary Table 4).

To identify additional actin-associated regulators, we treated cells with cytochalasin D, an agent that disrupts the actin network and induces the appearance of phalloidin-reactive filamentous foci[28]. By scoring transiently expressed RhoGEFs and RhoGAPs for their colocalization with these foci, we identified a total of 34 actin-associated proteins, only 12 of which were already known (Fig. 5b; Extended Data Fig. 6). Fittingly, the interactomes of these 34 RhoGEFs and RhoGAPs were enriched in actin-binding proteins ($P=1\times10^{-13}$, odds ratio = 7.2; Supplementary Table 3). Interestingly, CDC42 regulators were overrepresented on actin (Fig. 7c). These findings suggest that close proximity of dedicated RhoGEFs and RhoGAPs to actin is important to locally sense and control cytoskeletal dynamics.

Eleven regulators were localized to the nucleus in interphase cells. To assess whether these proteins are implicated in mitosis or cytokinesis following breakdown of the nuclear envelope, we analysed short interfering RNA (siRNA) screen data of MDA-MB-231 cells[29]. Indeed, depletion of these RhoGEFs or RhoGAPs led to a significant increase in multinucleated cells, which is a hallmark of cytokinesis failure, compared with the other non-nuclear-localized regulators in interphase ($P=9\times10^{-9}$, Wilcoxon test; Fig. 6a, Extended Data Fig. 7a).

Out of the 41 proteins tested, the position of the fluorescent tag affected the localization of only 3 proteins (Supplementary Table 4). However, examples of diverse isoform localizations were identified (Supplementary Information).

Our spatial mapping at steady-state does not consider potential stimulus-dependent or interaction-dependent relocalization of regulators. We therefore investigated the consequences of receptor tyrosine kinase signalling and determined which RhoGEFs and RhoGAPs are recruited by the central adaptor protein GRB2 to the epidermal growth factor receptor (EGFR). Five out of the 25 putative GRB2-interacting regulators tested were directly associated with the adaptor and were co-recruited to the plasma membrane following EGF stimulus (Fig. 6b; Extended Data Fig. 7b; Supplementary Table 4). Notably, they all predominantly resided in the cytosol without stimulus. Another example is the C-Dock subfamily of RhoGEFs (comprising DOCK6, DOCK7 and DOCK8), which were highly interconnected with the four members of the LRCH (leucine-rich repeat and calponin homology domain-containing) protein family[30] (Fig. 6c; Supplementary Table 3). The Dock proteins relocalize from the cytosol to sites of LRCH expression; that is, peripheral actin filaments and the endoplasmic reticulum (Fig. 6d–i; Extended Data Fig. 8). Given that RhoGEFs and RhoGAPs and their interactors are enriched for PDZ, SH2, WW and SH3 domains ($P<0.01$), which are common in scaffold or adaptor proteins, such recruitment probably affects the cellular distribution of other Rho regulators. These data suggest that ultimately, most, if not all, Rho regulation occurs on dedicated cellular structures.

Overall, we found 70% (99 out of 141) of the ectopically expressed RhoGEFs and RhoGAPs enriched at distinct subcellular compartments (Fig. 5c; Supplementary Table 4). The vast majority localized to structures previously shown to harbour Rho signalling. Our data provide a cellular heatmap of Rho regulation and suggest a critical role of RhoGEFs and RhoGAPs in conveying spatial context to Rho signalling control.

Focal adhesions are major sites of Rho GTPase regulation. To further resolve RhoGEF and RhoGAP localization to focal adhesions (FAs), which are key sites of cytoskeletal dynamics[31], we used total internal reflection fluorescence (TIRF) microscopy in flat COS-7 cells. Unexpectedly, we found that one-quarter of all regulators (37) associated with these structures (Fig. 7a; Supplementary Fig. 2). Previously, only eight RhoGEFs and RhoGAPs were proposed to form an integral part of the integrin adhesion network[32,33] (adhesome.org), of which we confirmed six (Supplementary Fig. 2). For 24 proteins identified in our screen, no evidence of FA localization existed in the literature. Interestingly, six regulators exhibited a pericentric enrichment juxtapositioned to FAs with a fluorescence intensity minimum in the centre (Fig. 7b; Supplementary Fig. 2). This result indicates the functional relevance of distinct microlocalizations around FA complexes. In support of our data, the interactomes of the FA-associated RhoGEFs and RhoGAPs were enriched in components of the adhesome ($P=2.5\times10^{-8}$, odds ratio = 2.3; Supplementary Table 3). Notably, RAC1 regulators were overrepresented on adhesions (Fig. 7c). Together, these data suggest that FAs are central sites of Rho signalling regulation.

Spatial segregation of RhoGEFs and RhoGAPs on FAs. We then explored the relevance of the FA association of RhoGEFs and RhoGAPs to the spatial organization of Rho signalling. Cell motility

Fig. 6 | RhoGEFs and RhoGAPs provide positional information to Rho signalling regulation. a, Implication of nuclear-localized RhoGEFs and RhoGAPs in cytokinesis. Distribution of *z*-scores for a number of multinucleated cells after genome-wide siRNA knockdown in MDA-MB-231 cells. Images of control (MOCK) and *TIAM2* RNA interference (siTIAM2) cells are shown as examples. Arrows indicate abnormal nuclei. Knockdowns were done in quadruplicate, and the *z*-scores were calculated against the mean of all measurements. **b**, Stimulus-dependent relocalization of RhoGEFs and RhoGAPs. Confocal micrographs of HeLa cells coexpressing EGFR-CFP, mRFP-GRB2 and indicated YFP-tagged regulators before (Pre) and 1 min after EGF stimulation. **c**, Left: C-Dock RhoGEFs and LRCH family proteins form a highly interconnected network. The thickness of nodes represents the *z*-score, and the interactome was derived from the 'bronze list' (Supplementary Table 3). Right: domain architecture of the human LRCH and C-Dock proteins. **d**, Live confocal micrographs of MDCK cells expressing the indicated YFP-tagged LRCH and C-Dock proteins alone, or indicated proteins together, revealing the recruitment of C-Dock RhoGEFs from the cytosol to the cell periphery by LRCH2. Line scans show colocalization of proteins. **e**, DOCK7 binds all four LRCH proteins. Representative IP of mCherry-DOCK7 with FLAG-tagged LRCH proteins or FLAG-Cherry control from HEK293T cell lysates. **f**, LRCH4 binds all C-Dock RhoGEFs, but not DOCK9. The DOCK-DHR2 domain is sufficient for binding. Representative IP of FLAG-LRCH4 with indicated mCherry-tagged Dock proteins or DOCK7-DHR2 fragment. **g**, The LRCH2 leucine-rich repeats probably mediate the interaction with DOCK8, while the CH domain is dispensable. Representative IP of YFP-DOCK8 with FLAG-tagged full-length LRCH2 or fragments. **h**, Upper: live confocal micrographs of MDCK cells coexpressing CFP-LRCH4 together with the ER marker PTP1B-YFP, revealing colocalization. Truncation of the putative LRCH4 transmembrane region (LRCH4-ΔTMR) causes its relocalization to the cell periphery. Lower: the CH domain of LRCH2 is sufficient for its targeting to the cell periphery. **i**, Cytochalasin D experiment (as in Fig. 5b), revealing actin association of a YFP-tagged LRCH2 CH domain fragment. Scale bars, 10 µm (**b**, **d**, **h** and **i**) or 50 µm (**a**). All confocal images are representative of three independent experiments. Data shown in **e**–**g** represent two independent experiments. Numerical source data and unprocessed blots are available in Source Data Fig. 6.

is coupled to cycles of RAC1-dependent lamellipodial protrusion at the leading edge and to RHOA-dependent myosin II contractility in the proximal lamella[17]. Consistently, recent studies of REF52 fibroblasts, a cell line frequently used for studying FA dynamics, have pointed to the existence of RAC1 and RHOA activity zones at the leading edge during isotropic cell spreading[20]. How protrusion–contraction cycles are spatially regulated and coupled to changes in mechanical tension in the cell is not understood. We therefore investigated whether adhesions act as scaffolds that specifically position GEFs and GAPs to control such activity zones. TIRF microscopy of isotropically spreading REF52 cells revealed a continuum of centripetally maturing adhesions[31] and remarkably distinct localization patterns of the regulators (Fig. 7d). Quantification of RhoGEF and RhoGAP fluorescence along these structures in concentric sampling regions (Fig. 7e,f; Extended Data Fig. 9a; Supplementary Fig. 3) and *z*-scoring and clustering of the normalized distributions (Fig. 7f) revealed a striking segregation of RAC1 regulators. While all RAC1-GAPs were enriched on mature FAs towards the cell centre, all RAC1-GEFs were preferentially targeted to peripheral adhesions. SRGAP1 and ARHGAP39, two RAC1-GAPs implicated in SLIT–ROBO signalling[34,35], were separately clustered. The four FA-binding RHOA-specific GAPs clustered less uniformly. Interestingly, the

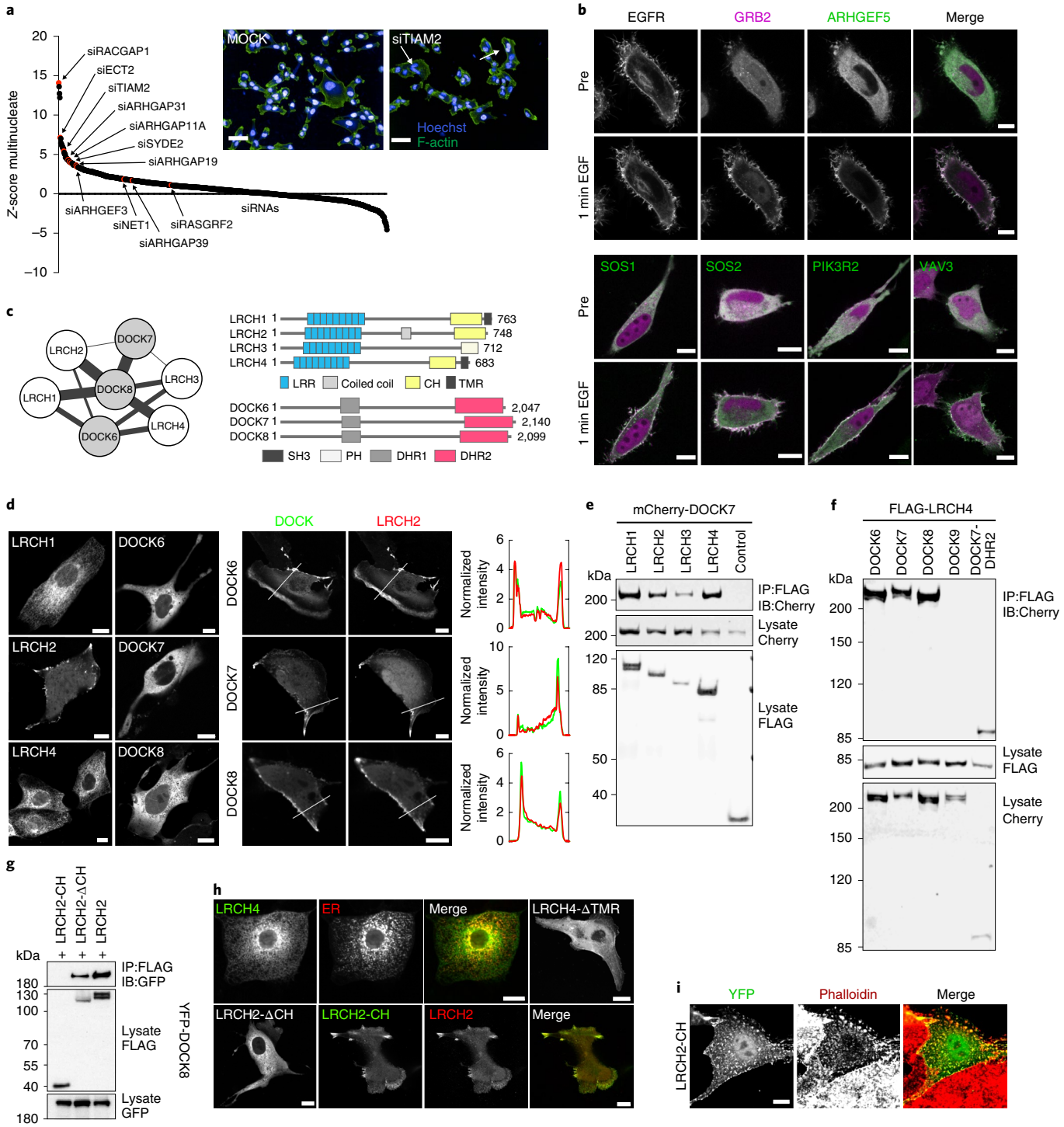

GAPs DLC1 and STARD13 accumulated in the periphery in a similar pattern to that of RAC1-GEFs. The only FA-localized RHOA-specific GEF in our screen, VAV3, was enriched towards the cell centre and clustered together with RAC1-GAPs. Notably, we did not find any other previously reported FA-localized RHOA-GEFs on these structures[36–39] (Supplementary Table 4). These results suggest a mechanism whereby FA scaffolds, presumably by relaying mechanical inputs to the FA-localized RAC1 regulators, spatially segregate GEF and GAP activity between the periphery and cell centre to shape the prominent leading-edge RAC1 activity zone[20,40].

Spatiotemporal RAC1 mechanosignalling from integrin adhesions. To understand how the positioning of regulators on adhesions generates Rho GTPase activity patterns and is coupled to mechanical forces in the cell, we used the Rho kinase inhibitor Y-27632 to perturb actomyosin contractility and reduce cytoskeletal tension. Y-27632 treatment caused increased protrusion and the disassembly of mature FAs[41] and led to the disappearance of the regulators from these structures. However, while the RAC1-GAPs remained largely cytosolic, all RAC1-GEFs accumulated on newly forming, edge-localized FA precursors (focal complexes (FCs)) (Supplementary Videos 1–6; Fig. 8a; Extended Data Fig. 10). This striking RAC1-GEF edge relocalization and the loss of RAC1-GAPs could explain the previously observed Y-27632-induced RAC1 activation at the leading edge[20]. This suggests that RAC1 regulators on integrin adhesions can directly translate the mechanical state of the cell into RAC1 activity patterns in migrating cells. The RHOA-GAPs DLC1 and STARD13 similarly accumulated on FCs. This pattern may further contribute to the control of the protrusion–contraction balance via reciprocal RHOA and RAC1 regulation[17,42].

Finally, we analysed adhesion-related RAC1 signalling modalities in post-spreading REF52 cells in a highly contractile state and imaged RAC1, CDC42 and RHOA biosensor activity on large mature FAs that accumulate at the cell periphery (Fig. 8b). To provide a high signal-to-noise ratio, we used oblique illumination microscopy to preferentially image the plasma membrane. We discovered a prominent reduction in RAC1 activity on FAs (Fig. 8b,c), which probably reflects the accumulation of RAC1-specific GAPs on mature FAs that are stabilized by the elevated contractile forces. By contrast, we did not observe any specific RHOA or CDC42 activity patterns at such FAs.

Our data suggest a role of RAC1-GEFs and GAPs in mechanosignalling. We propose that maturing integrin adhesions serve as spatially organizing platforms that enable these regulators to transduce mechanical cues from actomyosin into RAC1 activity patterns to control protrusion–contraction dynamics in migratory cells (Fig. 8d).

Discussion

Understanding how Rho GTPases spatiotemporally orchestrate morphodynamic processes is a long-standing challenge. A central question is how Rho signalling activity is established in narrow zones in cells while all involved proteins are subject to rapid entropic leakage. Recent studies have challenged the perception of Rho signalling as a 'GTPase-centric' process, with a static GTPase that is sequentially regulated by a GEF and GAP to control a single cytoskeletal structure[12–16].

Here, we provided a family-wide analysis of RhoGEFs and RhoGAPs that maps the cellular repertoire of context-specific Rho regulation and unveiled emergent organization principles of Rho signalling at the systems level. It establishes the framework for a 'regulator-centric' model in which RhoGEFs and RhoGAPs contextualize and spatially delimit the diffusional flux of Rho GTPases. They do so by providing positional information based on the placement of the enzymes on dedicated cellular structures and the assembly of additional signalling network components. Most regulators are autoinhibited, presumably due to the back-folding of adjacent regions onto the catalytic domains, thereby preventing access to substrates[43–45]. This suggests that RhoGEFs and RhoGAPs are poised to effectively respond to local regulation, a mechanism that further spatially confines their activity and allows rapid adaptation to changes in stimulus. Many regulators associate in collaborative networks, such as the PLEKHG4B–ARHGEF11–ARHGEF12 complex characterized here. This cooperativity, together with the promiscuity of the GEFs and GAPs, increases their combinatorial possibilities to control downstream signalling. It allows them to simultaneously engage multiple Rho GTPase family members and to precisely tune their activities. This also explains why the ectopic expression of RhoGEFs and RhoGAPs leads to a continuum of cell morphologies rather than the clear-cut cell shapes observed after global expression of activated forms of the GTPases[46] (Supplementary Information). Cooperativity also allows for tight coupling of Rho activation and inactivation, which can limit the spread of Rho activity zones and increase the responsiveness of the morphodynamic process[12]. Such interactions within similar protein classes have been described for phosphatases and kinases to interlink distinct types of cellular responses and to add robustness to signalling systems[47,48]. Diffusion spreads the active GTPases from the site of morphogenetic signalling.

Fig. 7 | Enrichment and spatial segregation of RhoGEFs and RhoGAPs on FAs. a,**b**, FA localization (**a**) and pericentric FA localization (**b**) of YFP-tagged RhoGEFs and RhoGAPs revealed by TIRF microscopy of COS-7 cells expressing the marker mCherry-paxillin. Right panels show longitudinal and transverse FA fluorescence intensity profiles of the white lines in the merged images on the left. Representative images of two independent experiments (with three images obtained for each experiment) with similar localization are shown. See Supplementary Fig. 2 for the full dataset. Scale bars, 5 µm (black) or 20 µm (white). **c**, RAC1-specific and CDC42-specific regulators are enriched on FA and actin, respectively. Odds ratios for enrichment of RhoGEFs and RhoGAPs with activity towards RHOA, RAC1 or CDC42 (as identified in the FRET screen, without ARHGAP42, ABR and BCR) on main subcellular locations are shown. Left: values are for regulators with exclusive substrate specificity (exclusive, 64 GEFs and GAPs), with any promiscuous or exclusive activity (active, 93 GEFs and GAPs) and for all active and non-active regulators (all, 138 GEFs and GAPs). Right: odds ratios for RAC1 regulators on FA with exclusive (exclus.) substrate specificity calculated separately for RhoGEFs and RhoGAPs. Broken lines indicate no enrichment at odds ratio = 1. *P* values were determined by two-sided Fisher's exact test. **d**, TIRF images of isotropically spreading REF52 cells grown on fibronectin expressing the indicated YFP-tagged proteins, showing their distribution on integrin adhesions as marked by mScarlet-dSH2 (a reporter for early and mature adhesions[65]). Normalized intensity at adhesions is false colour-coded according to the scale. Images are representative out of 10, 21 and 13 cells, with similar results obtained, for ARHGAP22, DOCK3 and paxillin, respectively. See Supplementary Fig. 3 for details and statistics. Scale bars, 10 µm. **e**, Quantification of the relative distribution of RAC1-specific GEFs and GAPs on adhesions (listed in Supplementary Table 5) in 0.8-µm sampling regions from the cell edge to the centre, and the remaining central region (see also Extended Data Fig. 9a and Supplementary Fig. 3). Means of $n = 9$–23 cells from one experiment are shown (see Supplementary Fig. 3 for details of *n*). Note that for RAC1-GAPs, co-transfection of RAC1-Q61L was required to balance GAP activity and induce proper cell spreading. RAC1-Q61L expression did not alter the protein distribution on adhesions (Extended Data Fig. 9b–e). For RAC1-GEFs and paxillin control, the plasma membrane marker K-Ras-HVR was co-transfected instead. **f**, Hierarchical clustering analysis heatmap of RhoGEF and RhoGAP distribution on adhesions, as in **b**. The *z*-scores were calculated from the mean of $n = 9$–23 cells from one experiment (see Supplementary Fig. 3 for details of *n*) for each sampling region across all analysed proteins. Numerical source data are provided in Source Data Fig. 7.

This is balanced by an efficient turnover of the GDP/GTP cycle, which is mediated by the action of RhoGAPs in the vicinity of the activated GTPases. We show that RhoGAPs are more promiscuous than RhoGEFs, a finding that is in agreement with previous biochemical studies of selected regulators[49,50]. RhoGAPs are also less interconnected in homotypic GAP–GAP complexes and have significantly fewer domains than RhoGEFs ($P=5\times10^{-4}$), and are therefore potentially more autonomous from regulation. Moreover, only

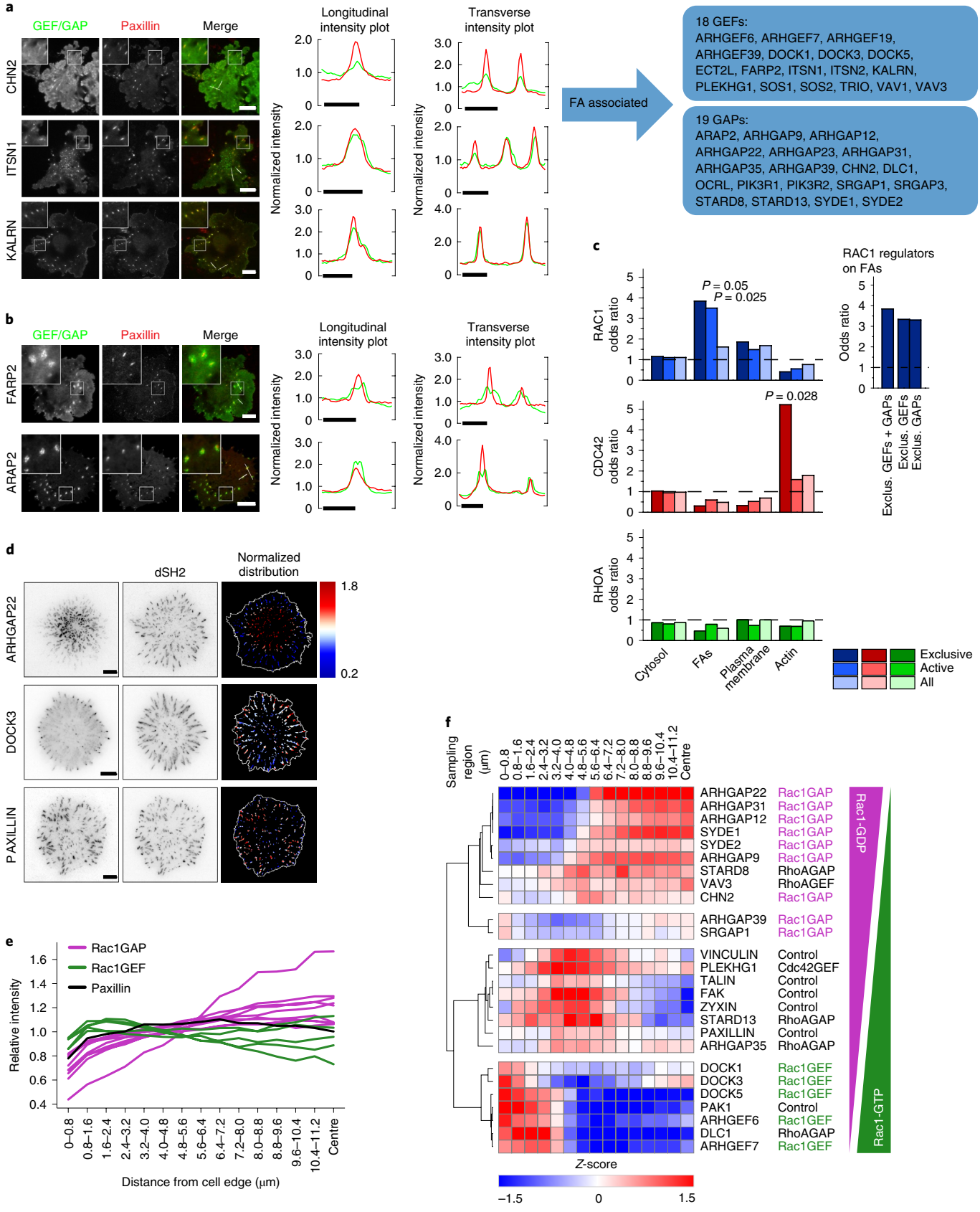

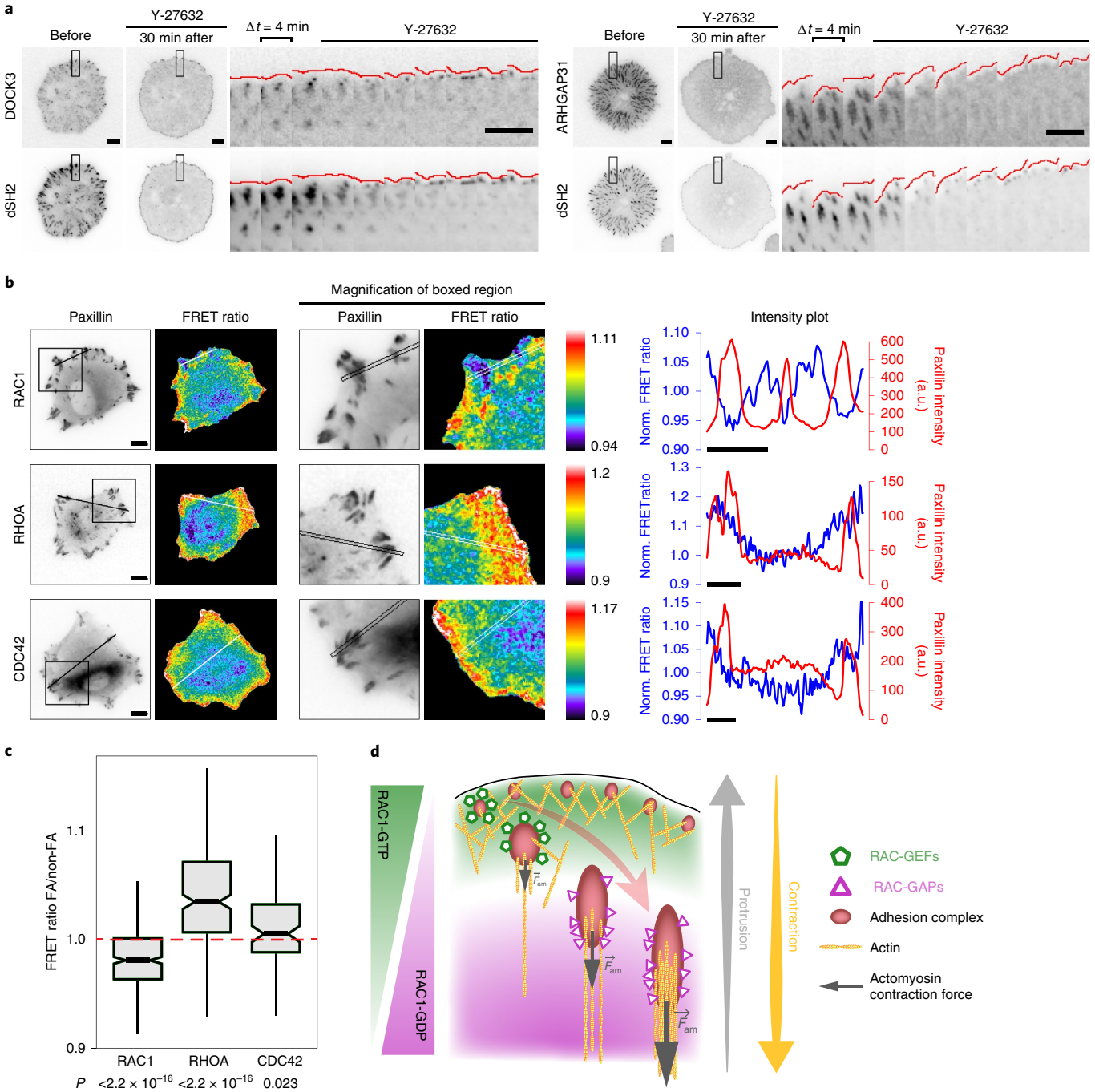

RhoGAPs localize to 'non-canonical' structures (comprising mitochondria, the Golgi, lysosomes, endomembranes and the endoplasmic reticulum) that are not primarily reported to host Rho signalling. Rho activity detected at these structures, for example, CDC42-GTP on the *trans*-Golgi[51], may be fuelled by passive transport of the activated GTPase to this site rather than by local GEFs. These properties may contribute to a housekeeping function of the RhoGAPs, which allows them to efficiently reset the GDP/GTP cycle and prevent signal leakage to the cell volume. This is reminiscent of other reaction cycles driven by the activities of opposing enzymes. Inactivating protein phosphatases, for example, also tends to display lower sequence selectivity than their activating kinase counterparts[52]. The efficient (re)cycling of Rho proteins through the confined activity zones essentially requires RhoGDIs, which sequester inactive Rho GTPases and facilitate their diffusional exploration of the cell.

Our activity screen focused on RHOA, RAC1 and CDC42. Seven other Rho family proteins are subject to similar GEF and GAP control[10,53] and are awaiting enzyme-substrate characterization.

The finding that integrin adhesions are spatially organizing platforms for the control of Rho signalling provides a mechanism for the transduction of mechanical cues into morphodynamic responses. Our data suggest that actomyosin forces are directly coupled to the presence and abundance of GEFs and GAPs on FAs and consequently to the spatiotemporal control of RAC1 at the leading edge. The spatial patterning of its activities thereby correlates with the distribution of protrusion and contraction processes, the key determinants of cell motility. Further studies are needed to reveal how the control of contractility via RHOA is coupled to this RAC1-regulating system on FAs. This will enhance our understanding of the antagonism of RHOA and RAC1 downstream of integrin

Fig. 8 | Spatiotemporal RAC1 mechanosignalling from integrin adhesions. a, Time-lapse images showing RhoGEF and RhoGAP redistribution on adhesions in isotropically spreading cells after Y-27632 addition (corresponding to Supplementary Videos 1 and 2). REF52 cells were treated as in Fig. 7d. Left: representative time points before and 30 min after addition of inhibitor. Right: kymographs of boxed regions on the left, with the cell edge marked in red. The RAC1-GEF DOCK3, but not the RAC1-GAP ARHGAP31, localizes to peripheral focal complexes after Y-27632 treatment (as indicated by the presence of dSH2 close to the cell edge). The data shown represent four and six independent experiments for DOCK3 and ARHGAP31, respectively. **b**, Left and middle: RAC1, RHOA and CDC42 activity on mature FAs of REF52 fibroblasts. Cells were transfected with RHOA-2G, RAC1-2G and CDC42-2G FRET sensors together with mCherry-paxillin, spread on fibronectin for >2 h and imaged by oblique illumination microscopy to bypass polluting signals from RhoGDI-bound, inactive Rho GTPase pools in the cytosol. Magnifications of boxed regions are shown in the middle panels. Right: intensity plots along the lines drawn in the images on the left show the distribution of the normalized FRET ratio (blue) and the paxillin intensity (red; given in arbitrary units (a.u.)). Representative examples of analysed cells are shown. **c**, Quantification of the experiment in **b**. FRET ratios were measured for individual cells in FAs, and the rest of the cell excluding FAs and spatial inhomogeneity is given as 'FRET ratio FA/non-FA'. The red broken line indicates no difference between FRET values in FA versus non-FA; a ratio >1 indicates higher Rho GTPase activity in FAs, while a ratio <1 indicate lower activity (data are from one experiment; for RAC1, $n = 366$ FAs in $n = 14$ cells; for RHOA, $n = 246$ FA in $n = 11$ cells, and for CDC42, $n = 87$ FAs in $n = 8$ cells). Boxplot centre lines represent the median values, box limits the 25th and 75th percentiles, and whiskers extend 1.5 times the interquartile range from the 25th and 75th percentiles. *P* values were calculated by Wilcoxon signed-rank test versus 1. **d**, Schematic showing that on maturing integrin adhesions, the segregation of RAC1-specific GEFs and GAPs between the cell periphery and centre generates spatiotemporal RAC1 activity patterns that control the protrusion–contraction dynamics in cells. Actomyosin mechanical forces (F_{am}) correlate with the stability of mature FAs and therefore the abundance of RAC1-GAP activity. Scale bars, 10 µm (**a** and **b**). Numerical source data are provided in Source Data Fig. 8.

activation. Future work will also show how the FA-associated GEFs and GAPs are functionally linked to other signalling programmes, for example, to those controlling cytoskeletal dynamics at the cell front or to mechanosensing modalities in more sophisticated morphogenetic processes, such as collective or three-dimensional migration[54,55]. Interestingly, RAC1 itself can associate with FAs and engage in additional feedback loops that may further tune its spatiotemporal activity[56,57]. The abundance of regulators on FAs could be exemplary for redundancy and diversity in the Rho GTPase regulatory system, with the existence of multiple GEF and GAP systems on these structures forming context-specific multiprotein complexes (as illustrated in our interactome data). Finally, it will be interesting to see whether other force-sensing structures, such as cell–cell adhesions, operate in a similar manner. The here-identified 34 actin-associated and 14 junctional RhoGEFs and RhoGAPs could be the starting point for such endeavours.

The mechanisms governing local Rho signalling fundamentally differ from those controlling the Ras GTPase system, which only involves about 16 GEFs and GAPs[58]. Here, spatial organization arises from cycles of lipid anchoring and membrane release of the Ras proteins[59–61]. The organization principles that emerged from this study therefore add to the growing landscape of reaction–diffusion mechanisms controlling localized activities of small GTPases and may apply to other important reaction cycles in signal transduction.

Online content

Any methods, additional references, Nature Research reporting summaries, source data, extended data, supplementary information, acknowledgements, peer review information; details of author contributions and competing interests; and statements of data and code availability are available at https://doi.org/10.1038/s41556-020-0488-x.

Received: 12 October 2018; Accepted: 18 February 2020;
Published online: 23 March 2020

References

1. Jaffe, A. B. & Hall, A. Rho GTPases: biochemistry and biology. *Annu. Rev. Cell Dev. Biol.* **21**, 247–269 (2005).
2. Heasman, S. J. & Ridley, A. J. Mammalian Rho GTPases: new insights into their functions from in vivo studies. *Nat. Rev. Mol. Cell Biol.* **9**, 690–701 (2008).
3. Porter, A. P., Papaioannou, A. & Malliri, A. Deregulation of Rho GTPases in cancer. *Small GTPases* **7**, 123–138 (2016).
4. Bos, J. L., Rehmann, H. & Wittinghofer, A. GEFs and GAPs: critical elements in the control of small G proteins. *Cell* **129**, 865–877 (2007).
5. García-Mata, R. & Burridge, K. Catching a GEF by its tail. *Trends Cell Biol.* **17**, 36–43 (2007).
6. Rossman, K. L., Der, C. J. & Sondek, J. GEF means go: turning on RHO GTPases with guanine nucleotide-exchange factors. *Nat. Rev. Mol. Cell Biol.* **6**, 167–180 (2005).
7. Tcherkezian, J. & Lamarche-Vane, N. Current knowledge of the large RhoGAP family of proteins. *Biol. Cell* **99**, 67–86 (2007).
8. DerMardirossian, C. & Bokoch, G. M. GDIs: central regulatory molecules in Rho GTPase activation. *Trends Cell Biol.* **15**, 356–363 (2005).
9. Garcia-Mata, R., Boulter, E. & Burridge, K. The 'invisible hand': regulation of RHO GTPases by RHOGDIs. *Nat. Rev. Mol. Cell Biol.* **12**, 493–504 (2011).
10. Aspenström, P. Fast-cycling Rho GTPases. *Small GTPases* https://doi.org/10.1080/21541248.2017.1391365 (2018).
11. Pertz, O. Spatio-temporal Rho GTPase signaling—where are we now? *J. Cell Sci.* **123**, 1841–1850 (2010).
12. Benink, H. A. & Bement, W. M. Concentric zones of active RhoA and Cdc42 around single cell wounds. *J. Cell Biol.* **168**, 429–439 (2005).
13. Machacek, M. et al. Coordination of Rho GTPase activities during cell protrusion. *Nature* **461**, 99–103 (2009).
14. Bravo-Cordero, J. J. et al. A novel spatiotemporal RhoC activation pathway locally regulates cofilin activity at invadopodia. *Curr. Biol.* **21**, 635–644 (2011).
15. Fritz, R. D. et al. A versatile toolkit to produce sensitive FRET biosensors to visualize signaling in time and space. *Sci. Signal.* **6**, rs12 (2013).
16. Graessl, M. et al. An excitable Rho GTPase signaling network generates dynamic subcellular contraction patterns. *J. Cell Biol.* **216**, 4271–4285 (2017).
17. Guilluy, C., Garcia-Mata, R. & Burridge, K. Rho protein crosstalk: another social network? *Trends Cell Biol.* **21**, 718–726 (2011).
18. Devreotes, P. & Horwitz, A. R. Signaling networks that regulate cell migration. *Cold Spring Harb. Perspect. Biol.* **7**, a005959 (2015).
19. Fritz, R. D. et al. SrGAP2-dependent integration of membrane geometry and slit-robo-repulsive cues regulates fibroblast contact inhibition of locomotion. *Dev. Cell* **35**, 78–92 (2015).
20. Martin, K. et al. Spatio-temporal co-ordination of RhoA, Rac1 and Cdc42 activation during prototypical edge protrusion and retraction dynamics. *Sci. Rep.* **6**, 21901 (2016).
21. Lawson, C. D. & Ridley, A. J. Rho GTPase signaling complexes in cell migration and invasion. *J. Cell Biol.* **217**, 447–457 (2018).
22. Cherfils, J. & Zeghouf, M. Regulation of small GTPases by GEFs, GAPs, and GDIs. *Physiol. Rev.* **93**, 269–309 (2013).
23. Eccles, R. L. et al. Bimodal antagonism of PKA signalling by ARHGAP36. *Nat. Commun.* **7**, 12963 (2016).
24. Yagi, H. et al. A synthetic biology approach reveals a CXCR4–G13–Rho signaling axis driving transendothelial migration of metastatic breast cancer cells. *Sci. Signal.* **4**, ra60 (2011).
25. Struckhoff, A. P. et al. PDZ-RhoGEF is essential for CXCR4-driven breast tumor cell motility through spatial regulation of RhoA. *J. Cell Sci.* **126**, 4514–4526 (2013).
26. Sternweis, P. C. et al. Regulation of Rho guanine nucleotide exchange factors by G proteins. *Adv. Protein Chem.* **74**, 189–228 (2007).
27. Diviani, D., Soderling, J. & Scott, J. D. AKAP-Lbc anchors protein kinase A and nucleates Gα12-selective Rho-mediated stress fiber formation. *J. Biol. Chem.* **276**, 44247–44257 (2001).
28. Schliwa, M. Action of cytochalasin D on cytoskeletal networks. *J. Cell Biol.* **92**, 79–91 (1982).
29. Pascual-Vargas, P. et al. RNAi screens for Rho GTPase regulators of cell shape and YAP/TAZ localisation in triple negative breast cancer. *Sci. Data* **4**, 170018 (2017).

30. Foussard, H. et al. LRCH proteins: a novel family of cytoskeletal regulators. *PLoS ONE* **5**, e12257 (2010).
31. Parsons, J. T., Horwitz, A. R. & Schwartz, M. A. Cell adhesion: integrating cytoskeletal dynamics and cellular tension. *Nat. Rev. Mol. Cell Biol.* **11**, 633–643 (2010).
32. Winograd-Katz, S. E., Fässler, R., Geiger, B. & Legate, K. R. The integrin adhesome: from genes and proteins to human disease. *Nat. Rev. Mol. Cell Biol.* **15**, 273–288 (2014).
33. Zaidel-Bar, R., Itzkovitz, S., Ma'ayan, A., Iyengar, R. & Geiger, B. Functional atlas of the integrin adhesome. *Nat. Cell Biol.* **9**, 858–867 (2007).
34. Lundström, A. et al. Vilse, a conserved Rac/Cdc42 GAP mediating Robo repulsion in tracheal cells and axons. *Genes Dev.* **18**, 2161–2171 (2004).
35. Wong, K. et al. Signal transduction in neuronal migration: roles of GTPase activating proteins and the small GTPase Cdc42 in the Slit–Robo pathway. *Cell* **107**, 209–221 (2001).
36. Guilluy, C. et al. The Rho GEFs LARG and GEF-H1 regulate the mechanical response to force on integrins. *Nat. Cell Biol.* **13**, 722–727 (2011).
37. Dubash, A. D. et al. A novel role for Lsc/p115 RhoGEF and LARG in regulating RhoA activity downstream of adhesion to fibronectin. *J. Cell Sci.* **120**, 3989–3998 (2007).
38. Lim, Y. et al. PyK2 and FAK connections to p190Rho guanine nucleotide exchange factor regulate RhoA activity, focal adhesion formation, and cell motility. *J. Cell Biol.* **180**, 187–203 (2008).
39. Iwanicki, M. P. et al. FAK, PDZ-RhoGEF and ROCKII cooperate to regulate adhesion movement and trailing-edge retraction in fibroblasts. *J. Cell Sci.* **121**, 895–905 (2008).
40. Kraynov, V. S. et al. Localized Rac activation dynamics visualized in living cells. *Science* **290**, 333–337 (2000).
41. Rottner, K., Hall, A. & Small, J. V. Interplay between Rac and Rho in the control of substrate contact dynamics. *Curr. Biol.* **9**, 640–648 (1999).
42. Lawson, C. D. & Burridge, K. The on-off relationship of Rho and Rac during integrin-mediated adhesion and cell migration. *Small GTPases.* **5**, e27958 (2014).
43. Rojas, R. J. et al. Gαq directly activates p63RhoGEF and Trio via a conserved extension of the Dbl homology-associated Pleckstrin homology domain. *J. Biol. Chem.* **282**, 29201–29210 (2007).
44. Canagarajah, B. et al. Structural mechanism for lipid activation of the Rac-specific GAP, beta2-chimaerin. *Cell* **119**, 407–418 (2004).
45. Mitin, N. et al. Release of autoinhibition of ASEF by APC leads to CDC42 activation and tumor suppression. *Nat. Struct. Mol. Biol.* **14**, 814–823 (2007).
46. Hall, A. Rho GTPases and the actin cytoskeleton. *Science* **279**, 509–514 (1998).
47. Breitkreutz, A. et al. A global protein kinase and phosphatase interaction network in yeast. *Science* **328**, 1043–1046 (2010).
48. St-Denis, N. et al. Phenotypic and interaction profiling of the human phosphatases identifies diverse mitotic regulators. *Cell Rep.* **17**, 2488–2501 (2016).
49. Jaiswal, M., Dvorsky, R. & Ahmadian, M. R. Deciphering the molecular and functional basis of Dbl family proteins: a novel systematic approach toward classification of selective activation of the Rho family proteins. *J. Biol. Chem.* **288**, 4486–4500 (2013).
50. Amin, E. et al. Deciphering the molecular and functional basis of RHOGAP family proteins: a systematic approach toward selective inactivation of RHO family proteins. *J. Biol. Chem.* **291**, 20353–20371 (2016).
51. Nalbant, P., Hodgson, L., Kraynov, V., Toutchkine, A. & Hahn, K. M. Activation of endogenous Cdc42 visualized in living cells. *Science* **305**, 1615–1619 (2004).
52. Smoly, I., Shemesh, N., Ziv-Ukelson, M., Ben-Zvi, A. & Yeger-Lotem, E. An asymmetrically balanced organization of kinases versus phosphatases across eukaryotes determines their distinct impacts. *PLoS Comput. Biol.* **13**, e1005221 (2017).
53. Jaiswal, M., Fansa, E. K., Dvorsky, R. & Ahmadian, M. R. New insight into the molecular switch mechanism of human Rho family proteins: shifting a paradigm. *Biol. Chem.* **394**, 89–95 (2013).
54. ten Klooster, J. P., Jaffer, Z. M., Chernoff, J. & Hordijk, P. L. Targeting and activation of Rac1 are mediated by the exchange factor beta-Pix. *J. Cell Biol.* **172**, 759–769 (2006).
55. Chang, F., Lemmon, C. A., Park, D. & Romer, L. H. FAK potentiates Rac1 activation and localization to matrix adhesion sites: a role for βPIX. *Mol. Biol. Cell* **18**, 253–264 (2007).
56. Friedl, P., Sahai, E., Weiss, S. & Yamada, K. M. New dimensions in cell migration. *Nat. Rev. Mol. Cell Biol.* **13**, 743–747 (2012).
57. Kutys, M. L. & Yamada, K. M. An extracellular-matrix-specific GEF–GAP interaction regulates Rho GTPase crosstalk for 3D collagen migration. *Nat. Cell Biol.* **16**, 909–917 (2014).
58. Hennig, A., Markwart, R., Esparza-Franco, M. A., Ladds, G. & Rubio, I. Ras activation revisited: role of GEF and GAP systems. *Biol. Chem.* **396**, 831–848 (2015).
59. Rocks, O. et al. The palmitoylation machinery is a spatially organizing system for peripheral membrane proteins. *Cell* **141**, 458–471 (2010).
60. Lorentzen, A., Kinkhabwala, A., Rocks, O., Vartak, N. & Bastiaens, P. I. H. Regulation of Ras localization by acylation enables a mode of intracellular signal propagation. *Sci. Signal.* **3**, ra68 (2010).
61. Schmick, M. et al. KRas localizes to the plasma membrane by spatial cycles of solubilization, trapping and vesicular transport. *Cell* **157**, 459–471 (2014).
62. Sterpetti, P. et al. Activation of the Lbc Rho exchange factor proto-oncogene by truncation of an extended C terminus that regulates transformation and targeting. *Mol. Cell. Biol.* **19**, 1334–1345 (1999).
63. Chikumi, H. et al. Homo- and hetero-oligomerization of PDZ-RhoGEF, LARG and p115RhoGEF by their C-terminal region regulates their in vivo Rho GEF activity and transforming potential. *Oncogene* **23**, 233–240 (2004).
64. Banerjee, J., Fischer, C. C. & Wedegaertner, P. B. The amino acid motif L/IIxxFE defines a novel actin-binding sequence in PDZ-RhoGEF. *Biochemistry* **48**, 8032–8043 (2009).
65. Kirchner, J., Kam, Z., Tzur, G., Bershadsky, A. D. & Geiger, B. Live-cell monitoring of tyrosine phosphorylation in focal adhesions following microtubule disruption. *J. Cell Sci.* **116**, 975–986 (2003).

Publisher's note Springer Nature remains neutral with regard to jurisdictional claims in published maps and institutional affiliations.

© The Author(s), under exclusive licence to Springer Nature Limited 2020

Methods

Cloning of RhoGEF and RhoGAP cDNA expression library. After scanning all human sequences (UniProt, 2015) with the Pfam[66] HMM models for the RhoGAP, RhoGEF and DHR-2 domains using the hmmsearch function from the HMMER package[67], 145 RhoGEFs and RhoGAPs were identified. A total of 141 full-length cDNAs were curated through the MGC/ORFeome collection, the Kazusa DNA Research Institute collection, gene synthesis (33 cDNAs, GenScript), the contribution by authors of previously published materials and cloning from cDNA libraries. A total of 116 out of 141 cDNAs matched the longest predicted isoform. A total of 25 cDNAs represented slightly shorter forms, which, on average, lacked only 3% of the full-length size. cDNAs were from human (112), mouse (26), rat (2) and chimpanzee (1) genes. Expression libraries of mCitrine-YFP and mCherry fusion proteins were generated using a modified Creator donor plasmid system with flanking AscI and PacI restriction sites[68] or the Gateway system (Thermo Fisher) (Supplementary Table 1; Extended Data 1). All mutation and deletion constructs were created by site-directed mutagenesis (Agilent Technologies). To maintain potential carboxy-terminal PDZ-binding motifs present in 52 RhoGEFs and RhoGAPs (37%)[5] (Supplementary Table 4), stop codons were introduced into the PacI site.

Mammalian cell culture. HEK293T, HEK293, COS-7, HeLa and REF52 cells were grown in DMEM (Thermo Fisher), and MDCK cells were grown in modified Eagle medium (Thermo Fisher), supplemented with 10% fetal bovine serum (FBS, Biochrom) and 100 U ml^{-1} penicillin–streptomycin (Thermo Fisher) unless directed otherwise. HEK293T cells were transfected using polyethylenimine (Polysciences), MDCK cells were transfected using Effectene (Qiagen), and COS-7, HeLa and REF52 cells were transfected using Lipofectamine 3000 (Thermo Fisher). Stable RhoGDI-knockdown HEK293T cells were generated using the following lentiviral short hairpin RNA (shRNA) target sequences: CGTCTAACCATGATGCCTTAA (shRNA1; NM_004309.3-1198s1c1; the RNAi Consortium (TRC)) or CAAGATTGACAAGACTGACTA (shRNA2; NM_004309.3-503s1c1). The mCherry-paxillin COS-7 cell line was generated by lentiviral infection with a mCherry-paxillin Gateway expression construct under the control of the ubiquitin C promoter (provided by A. Löwer, TU Darmstadt).

Immunoprecipitation and western blotting. HEK293T cells were lysed in NP40 lysis buffer (1% NP40, 20 mM Tris-HCL (pH 7.5), 150 mM NaCl, 1 mM EGTA, 5 mM NaF) with complete protease inhibitor cocktail (Roche) and *N*-ethylmaleimide (Sigma). For immunoprecipitation, cleared lysates were added to either FLAG-M2 affinity gel (Sigma) or protein G sepharose beads (Sigma) coupled with anti-green fluorescent protein (GFP; ab290, Abcam). After 1 h of rotation (4 °C), beads were washed three times in lysis buffer and eluted with Laemmli buffer. The following antibodies were used for western blotting: FLAG (Sigma, M2; 1:5,000); GFP (Abcam, ab290; 1:10,000); RhoGDI (Santa Cruz, sc360; 1:2,000); α-tubulin (Sigma, DM1a; 1:10,000); and mCherry (Abcam, ab125096; 1:2,000). Protein bands were detected either by chemiluminescence or using a LI-COR Odyssey imaging system (LI-COR Biosciences).

FRET biosensor-based RhoGEF and RhoGAP activity assay. HEK293T cells were seeded in poly-L-lysine-coated (25 ng µl^{-1}) 96-well plates (µ-Plate, ibidi) in FluoroBrite DMEM (Thermo Fisher) supplemented with 10% FBS and allowed to adhere overnight. For the RhoGEF screen, wild-type HEK293T cells were transfected with 40 ng of FRET sensor, 80 ng of RhoGDI or mCherry control, and 280 ng of RhoGEF or mCherry control. For the RhoGAP screen, RhoGDI-knockdown HEK293T cells (shRNA2; Extended Data Fig. 2c–e) were transfected with 30 ng of FRET sensor and 270 ng of RhoGAP or mCherry control. After 24 h, the medium was replaced with FluoroBrite DMEM supplemented with 1% FBS. Cells were imaged 48 h after transfection. For autoinhibition experiments, the transfected ARHGEF5 isoform2 and ARHGEF16 isoform2 plasmids were reduced to 60 ng and 70 ng, respectively (filled to 280 ng with empty vector), to adjust their expression levels to those of the corresponding longer isoforms. For the PLEKHG4B, ARHGEF11 and ARHGEF12 FRET experiments, cells were transfected with 40 ng of FRET sensor, 80 ng of RhoGDI or mCherry control, 140 ng of mCherry-labelled RhoGEF or mCherry control and 140 ng of miRFP670-labelled RhoGEF mutants or truncations or miRFP670 control. For titration experiments, total DNA levels were filled to the same amount with mCherry or miRFP670 plasmid.

FRET experiments were performed on an Olympus IX81 microscope equipped with an UPLSAPO ×10/0.4 numerical aperture (NA) air objective, a MT20 150 W xenon arc burner light source (Olympus) and a temperature-controlled incubation chamber to maintain 37 °C, 5% CO_2 and 60% humidity. Images were acquired with a water-cooled EMCCD camera (Hamamatsu) at 16-bit depth. The following combinations of excitation filters (Ex), dichroic mirrors (DM) and emission filters (Em) were used: donor channel Ex: 430/25, DM: zt442RDC, Em: 483/32; FRET-acceptor channel Ex: 430/25, DM: zt442RDC, Em: 542/27; acceptor/mVenus channel Ex: 500/20, DM: zt514RDC, Em: 542/27; mCherry channel Ex: 572/23, DM: HC BS 593, Em: 623/24; miRFP670 channel Ex: 640/30, DM: R405/488/561/635, Em: 692/40. Five fields of view were imaged for each condition in each of the above channels and transmission light channel.

Raw image datasets were processed using a custom Fiji script. First, raw images were smoothed by Gaussian filter convolution with a radius of 1 pixel and then background-corrected by subtracting the average background images. Regions of interest were generated based on the acceptor channel, the mCherry channel and, where needed, miRFP670 channel images, and low-intensity pixels from donor and FRET-acceptor channels were excluded. FRET ratio (R) images were created by dividing the FRET-acceptor channel by the donor channel image on a pixel basis. Within the region of interest, average intensities of the FRET ratio image and images of the acceptor, mCherry and miRFP670 channels were measured.

Average FRET ratios of five fields of view were normalized to control. For the RhoGEF screen, four control wells were averaged per plate, while for the RhoGAP screen, three control wells. Thresholds to assign RhoGEF and RhoGAP activities were defined as a multiple of the standard deviation (σ) of control+RhoGDI (RhoGEF screen) or control (RhoGAP screen), based on the following precision recall analysis benchmarks: $1+3\sigma$ of control+RhoGDI for RHOA (1.0619), $1+1.5\sigma$ of control+RhoGDI for RAC1 (1.0121), $1+1.7\sigma$ of control+RhoGDI for CDC42 (1.016) for the RhoGEF screen and $1-4\sigma$ of control (0.9265) for RHOA, $1-4\sigma$ of control (0.9603) for RAC1, $1-2\sigma$ of control (0.9779) for CDC42 for the RhoGAP screen.

For direct comparison of the catalytic activities of a given RhoGEF or RhoGAP towards the three GTPases tested, the change in FRET ratio compared to control+RhoGDI (RhoGEF screen) or control (RhoGAP screen) (ΔR) was normalized to the maximal observed FRET ratio change (ΔR_{MAX}). For RhoGEFs and RhoGAPs with activity towards multiple substrates, only those above 20% of the main substrate activity were taken into account.

To assess potential autoinhibition activities of RhoGEFs and RhoGAPs by semiquantitative FRET analysis, changes in FRET ratio (R) compared to control+RhoGDI (RhoGEF screen) or control (RhoGAP screen) were calculated (ΔR). The RhoGEF or RhoGAP mCherry intensities were then normalized to the mCherry control intensities, and the ΔR of each of the two regulator constructs were then each divided by their corresponding normalized mCherry intensities.

Literature survey of RhoGEF and RhoGAP specificities. Information from 450 publications with claims of catalytic activities of RhoGEFs and RhoGAPs towards RHOA, RAC1 and CDC42 was collected. Since the resulting 'integrated' specificity list (Supplementary Table 2) was highly inconsistent owing to differences in the experimental approaches used (Supplementary Information), separate datasets for activities detected in vitro and in vivo were generated. An entry of a regulator in these lists ('activity' or 'no activity' towards the three GTPases) was only accepted if either no conflicting study existed or a conflicting report could be overruled by three consistent studies. Finally, a 'reference list' was generated that excludes mismatches between the in vitro and in vivo lists.

RhoGEF and RhoGAP interactome acquisition and analysis. *Sample preparation and MS.* 3×FLAG-tagged and mCitrine-YFP-tagged RhoGAP and RhoGEF expression plasmids were transiently transfected into HEK293T cells and, separately, stably integrated mCitrine-YFP-tagged RhoGEF and RhoGAP constructs into HEK293 cells. Cells were lysed in NP40 buffer and proteins were isolated using anti-FLAG M2 (Sigma) or packed GFP-trap (Chromotek) sepharose beads following standard procedures (Supplementary Information). Samples were processed using a solid-phase digest protocol using proteomic reactors[69] or spin-tips. A subset of samples (search task numbers 285 and 748) were digested 'on-bead' (Biostudies:S-BSST160; Supplementary Information).

Digested samples were processed on a ThermoFisher LTQ linear ion trap, a ThermoFisher LTQ-Orbitrap or a SCIEX TripleTOF 5600 (Biostudies:S-BSST160) as detailed in the Supplementary Information. Data were acquired in a data-dependent manner. MS/MS spectra were searched against the latest human proteome at the time (RefSeq (v.42 and v57)[70]) using the Mascot (Matrix Science) spectral matching program. Search engine results from each run were submitted to the ProHits platform[71]. Conversion and Mascot parameters are detailed in Biostudies:S-BSST160.

For samples submitted to PRIDE under the accession PXD010084 (Biostudies:S-BSST160), proteins were digested on-beads with trypsin as previously described[72] and desalted using the stage-trip protocol[73] (Supplementary Information). MS acquisition occurred in the data-dependent mode using the top 20 peaks for MS2 fragmentation at a resolution of 70,000 for MS1 and 15,000 for MS2 and a maximum injection time of 100 ms for MS2. Database searching was performed using MaxQuant (v.1.5.2.8)[74], with oxidized methionine, deamidation on asparagine and glutamine as well as acetylated N termini as variable modifications and carbamidomethylation as a fixed modification against a human UniProt database (2017-01) and a peptide and protein false discovery rate (FDR) cut-off value of 1%. We performed protein-level quantitation using the MaxLFQ algorithm[75] with the match-between-runs option turned on without requiring MS2 for LFQ comparisons.

Interactome network construction. For data filtering, false positives carried over from previous samples were removed. Total peptide counts were then normalized by protein sequence length. To increase the score weight of prey from better quality runs, the normalized prey total peptide counts were multiplied by that of

the corresponding bait. To identify proteins that were statistically more abundant as prey of specific baits (in specific samples), only prey with normalized counts greater than the upper limit of the 99% prediction interval were kept using their distribution across all samples as background. For bait–prey combinations tested in multiple replicates, the top two normalized prey counts were averaged for the background distribution. A frequency and Mascot score cut-off was then defined that achieved a precision greater than 75% (7% and log(score) = 6.3 respectively; positive dataset: HIPPIE database[76], negative dataset: negative controls). Prey were removed if they did not meet these cut-off values and appeared in the CRAPome database[77] with a positive score. A FDR (based on DECOY sequences) of less than 1% was also a MASCOT cut-off score requirement. Additionally, prey appearing with fewer than three total unique peptides across bait samples were removed as interactors of these baits. The resulting list constitute the 'bronze list' of interactions. Finally, the ComPASS *z*-score[78] was calculated and a silver cut-off was defined (minimum precision of 70%) as well as a gold cut-off (maximum Matthew correlation coefficient). Samples processed by different machines were separately treated. The code for this analysis can be found at https://gitlab.ebi.ac.uk/petsalaki/the-rhome. The amount of data generated from the baits analysed by a Q Exactive HF-X instrument (see above) were insufficient to create a background distribution or to calculate the 99% prediction interval, as were the number of known true interactions. As at least two replicates for these runs existed, SAINTexpress[79] was applied and the following parameters were required: a cut-off value >0.3 for the SAINT score, a *z*-score >1, a bait sequence coverage of at least 15% and a project frequency <50%. This latter cut-off seems lenient, but several of our baits interacted with each other in this set (Extended Data Fig. 4) and therefore had a high project frequency. Finally, all interactome datasets were merged, the project frequency recalculated over the entire project and prey with a frequency >10% were removed.

Pathway enrichment. Pathway enrichment analysis (Extended Data Fig. 3a) was performed using ReactomePA[80]. Pathways were merged if they had a highly overlapping Pearson's correlation of components value of >0.7. Clustering was done using the hclust function in R[81].

Interactome quality. Quality control of our interactome was done by comparing our data to Bioplex 2.0 (ref. [82]). Only open reading frames that had a similar sequence length (±10%) to our constructs were used (Supplementary Information). Interactions were compared to the IntAct database[83] for 'novelty'. For calculation of the tissue-specific coexpression of binding partners, GTEx v.7 was used (www.gtexportal.org; dbGaP accession phs000424.v7.p2). The background set comprised 5,000×5,000 random protein pairs, and significance was tested using two-tailed Wilcoxon tests.

SRE.L luciferase assay. Rho GTPase activity was assessed using the Rho-pathway-selective SRE.L luciferase reporter as previously described[84]. HEK293T cells on 12-well tissue culture plates were co-transfected with 200 ng of pGL4.34 SRE.L firefly reporter, 20 ng of pRL-CMV Renilla luciferase reporter (used as a control for transfection efficiency) and 50 ng of 3×FLAG-tagged RhoGEF expression constructs. The total amount of transfected DNA was kept constant between wells by adjustment with 3×FLAG empty vector. At 16–20 h post transfection, cells were lysed in 140 µl NP40 lysis buffer containing complete protease inhibitor (Roche) and 1 µg ml^{-1} Dnase I (New England BioLabs) for 20 min at 4 °C on a rocking shaker. Transcription levels of Renilla and firefly luciferase were measured using a Dual-Glo Luciferase Assay System (Promega) following the manufacturer's instructions, using 20 µl of lysate in a 96-well white flat-bottom microplate (Greiner Bio One) in an Infinite M200 PRO plate reader (Tecan). Firefly luminescence intensity was normalized to Renilla luminescence intensity. After taking aliquots for the luciferase assay, lysates of triplicates were pooled for analysis of protein expression by western blotting.

G-LISA assay. RHOA, RAC1 and CDC42 G-LISA kit activity assays (Cytoskeleton) were performed according to the manufacturer's instructions. In brief, 20 h after transfection, HEK293T cells were washed in ice-cold PBS, lysed with G-LISA kit lysis buffer and centrifuged. Aliquots for estimating protein concentration were collected, and remaining lysates were snap-frozen in liquid nitrogen. A total of 0.5 mg ml^{-1} of protein was subsequently used per condition in the assay.

Confocal microscopy localization screen. MDCK cells seeded on glass-bottom dishes (MatTek) were live-imaged 24 h post transfection on a Fluoview 1000 confocal microscope (Olympus) equipped with a UPLSAPO_60/1.3 NA silicon immersion oil lens using the following Ex and Em settings: mCerulean-CFP Ex: 440 nm, Em: 460–500 nm; GFP, AlexaFluor488 Ex: 488 nm, Em: 500–545 nm; mCitrine-YFP, Venus-YFP Ex: 515 nm, Em: 530–545 nm; AlexaFluor555 Ex: 559 nm, Em: 570–625 nm; mCherry Ex: 559 nm, Em: 575–675 nm; AlexaFluor647 Ex: 635 nm, Em: 655–755 nm. Images were also acquired using a Nikon/Andor CSU-W spinning disk microscope equipped with a ×100 oil CFI P-Apo λ/NA 1.45/WD 0.13 objective and an Andor iXON DU-888 EMCCD using the following settings: mCerulean-CFP Ex: 445 nm, Em: 460–500 nm; mCitrine-YFP Ex: 514 nm, Em: 542–576 nm; mCherry Ex: 561 nm, Em: 582–636 nm; AlexaFluor647 Ex 637 nm, Em: 665–705 nm. For GRB2 translocation experiments, HeLa cells were imaged by time-lapse microscopy before and after the addition of 100 ng ml^{-1} EGF.

TIRF microscopy screen. COS-7 cells were reverse transfected and seeded on glass-bottom dishes (MatTek). Images were taken 15–20 h post transfection at 37 °C on an Olympus IX81 microscope equipped with an APON ×60/1.49 NA oil immersion TIRF objective and a motorized four-line TIRF condenser (Olympus) using a water-cooled EMCCD camera (Hamamatsu) at 16-bit depth. The following Ex and Em settings were used: mCitrine-YFP, mEGFP Ex: 488 nm, Em: 525/50; mCherry Ex: 561 nm, Em: 617/73; miRFP Ex: 640 nm, Em: 692/40. Fluorescence intensity line scans were generated using the plot profile tool in Fiji. The pixel intensity was averaged on a line width of 3 pixels and normalized to the average intensity along the selection.

Cytochalasin D assay. MDCK cells on glass coverslips were transfected with mCitrine-YFP-tagged RhoGEF or RhoGAP library constructs, treated for 30 min at 37 °C with 50 µM cytochalasin D (Focus Biomolecules), fixed with 4% paraformaldehyde, permeabilized with 0.2% Triton X-100/100 mM glycine and blocked in 3% BSA. GFP primary antibody (Abcam, ab13970; 1:1,000) incubation was performed at 4 °C overnight, and Alexa Fluor488 secondary antibodies (Molecular Probes, A11039, 1:1,000) were incubated for 30 min. CF568 Phalloidin conjugate (Biotium) to stain actin filaments was added to the secondary antibody mixture. Coverslips were mounted using ProLong Gold (Invitrogen).

Spatial segregation analysis of RhoGEFs and RhoGAPs on FAs. REF52 fibroblasts were reverse transfected 15–20 h before imaging. Cells were trypsinized, allowed to recover for 10 min and seeded on fibronectin-coated (25 µg ml^{-1}) glass (µ-Slide glass bottom, ibidi) in FluoroBrite DMEM supplemented with 10% FBS. After 30–80 min of seeding, images were taken using a TI2-E inverted microscope (Nikon) equipped with a spinning TIRF illumination unit (VectorTIRF, 3i), a CFI Apo ×60/1.49 NA oil TIRF objective (Nikon) and an ImagEM X2 EM-CCD camera (Hamamatsu) at 37 °C and 5% CO_2. Images were analysed using a custom-made script in Fiji. Images were corrected by dark-current subtraction and flat-field correction. Adhesion complexes and cell outlines were segmented using mScarlet-dSH2 and iRFP-RAC1-Q61L or miRFP-KRas-HVR channels, respectively. mCitrine-YFP fluorescence intensity at adhesion complexes was normalized to the average intensity at these structures and quantified from the cell edge to the cell centre 14 times in 0.8-µm sampling regions and in the remaining centre region. Relative intensities of sampling regions were averaged across $n = 9–23$ cells, and the *z*-score was calculated for each sampling region across all analysed proteins. Hierarchical clustering analysis was performed in Morpheus (https://software.broadinstitute.org/morpheus) based on 1-pearson correlation using average linkage. For Y-27632 experiments, REF52 cells were treated as described above and imaged by time-lapse spinning TIRF recording. Y-27632 (10 µg ml^{-1}) was added 40 min after seeding.

FA biosensor analysis. At 2 h before imaging, REF52 cells were reseeded into black 6-well glass-bottom plates (Cellvis, p06-1.5H-N) coated with 10 µg ml^{-1} fibronectin (Cornwell). Imaging was performed in phenol-red free DMEM (Sigma) containing 0.5% FBS (Sigma), 0.5% BSA (Sigma) and 4 mM L-glutamine (Sigma). Live-cell microscopy was performed at 37 °C using laser-based autofocus on an Eclipse Ti inverted fluorescence microscope (Nikon) with a Plan Apo VC λ oil ×60/1.4 NA objective controlled by MetaMorph (Molecular Devices). For oblique illumination imaging, 440-nm or 561-nm solid-state laser diodes integrated within a modular TIRF system were used (ILAS2, Roper Scientific). FRET/mCherry illumination experiments were performed using an Andor Zyla 4.2 plus (USB3.0) camera. All images were acquired with 2×2 binning at 16-bit depth.

FRET data were analysed as described elsewhere[15]. FA structures were thresholded and used as masks based on the mCherry-paxillin signal using a custom-made script in Python 3.0 (http://www.python.org). FA structures that were >50 pixels in size were included in the analysis to ensure the analysis of mature FAs and to exclude non-FA elements such as vesicular organelles. Data analyses, processing and graphical visualization were performed in R (http://www.R-project.org/).

High-content imaging. COS-7 cells were plated in duplicate in 384-well plates and transfected with mCitrine-YFP-tagged RhoGEF or RhoGAP constructs or empty mCitrine vector. Cells were fixed and permeabilized using 0.2% Triton X-100/PBS for 15 min and incubated in 0.5% FBS/PBS for 1 h. Cells were incubated with the primary antibodies mouse anti-α-tubulin (Thermo Fisher, A11126; 1:1,000) and rabbit anti-GFP (Molecular Probes, A11122; 1:5,000) in 0.5% FBS/PBS overnight at 4 °C and with the secondary antibodies Alexa Fluor647 goat anti-mouse (Molecular Probes, A21237; 1:500) and Alexa Fluor488 goat anti-rabbit (Molecular Probes, A11008; 1:500) in 0.5% FBS/PBS for 1 h. Finally, cells were incubated with 10 µg ml^{-1} 4,6-diamidino-2-phenylindole (DAPI)/PBS (Thermo Fisher) for 15 min and washed twice in PBS. All steps were performed at room temperature, including three washes in PBS before each step.

Cells were imaged at ×20 magnification using an Opera High Content Screening System (Perkin Elmer) (35–40 images per well; Biostudies:S-BSST160). Columbus Image Analysis software (Perkin Elmer) was used to segment images and to detect cells. Poorly segmented or incompletely imaged cells were filtered

out, and transfected cells were identified by their anti-GFP staining. A total of 236 features quantitatively describing cell and nuclear morphology, DAPI, α-tubulin and GFP staining intensities and textures of transfected cells were analysed (Biostudies:S-BSST160). *Z*-scores were calculated as follows: $Z = (\text{well mean score} - \text{YFP control well mean score})/\text{YFP control well standard deviation}$ (Biostudies:S-BSST160).

Statistics and reproducibility. The FRET-based RhoGEF and RhoGAP activity assay was run in three independent replicates, and the statistical significance of all values above and below the threshold (RhoGEF and RhoGAP screen respectively) was calculated using unpaired two-sided Student's *t*-tests (observed versus control+RhoGDI (RhoGEF screen) or observed versus control (RhoGAP screen)). To prevent alpha error accumulation as a result of multiple hypothesis tests, the Benjamini–Hochberg correction was applied as a FDR-controlling procedure, with $\alpha = 0.05$.

When calculating the enrichment of a feature in our interactome, we used 10,000 iterations of a randomized network, derived from Bioplex 2.0 (ref. [78]), as background, which maintained the size and degree distribution of our network. When comparing enrichment of localizations, the Cell Atlas study or data from Simpson et al.[85] were used as background, as described in the main text. The enrichment was calculated using the fisher.test function in R. To compare the domain compositions of RhoGAPs and RhoGEFs, the distribution of the domain numbers for RhoGAPs versus RhoGEFs was calculated using two-tailed Wilcoxon tests (RhoGAPs: 3.2 ± 2.4 versus RhoGEFs: 4.9 ± 3.6, $P = 5 \times 10^{-4}$). To identify actin-binding proteins in our interactome, the keywords 'actin binding proteins' were used to search the UniProt database (UniProt, 2015; Biostudies:S-BSST160). FA-associated proteins were extracted from the adhesome.org database[33] (Biostudies:S-BSST160). Odds ratio and two-tailed Fisher's exact tests were calculated based on 2×2 contingency tables.

To determine the RhoGEFs and RhoGAPs that contribute to cytokinesis, a dataset comprising images of single MDA-MB-231 cells following genome-wide knockdown was analysed[29]. Briefly, the percentage of multinucleated cells was calculated in each RNA-interference-treated cell population from each well by first identifying multinucleated cells using the 'M' nuclear segmentation algorithm of the Columbus Image Analysis tool (PerkinElmer), and then dividing this number by the total number of cells in the well. For each well a *z*-score was calculated based on the mean percentage of multinucleated cells of the well. The enrichment was calculated by assessing whether depletion of nuclear RhoGEFs and RhoGAPs resulted in significant increases in the percentage of multinucleated cells (based on *z*-scores) compared with non-nuclear RhoGEFs and RhoGAPs (Wilcoxon test, two-tailed).

For all other data, data are represented as the mean ± s.d., and statistical analyses were performed using unpaired two-sided Student's *t*-tests, unless otherwise noted. Differences in the mean were considered significant at $P < 0.05$. In Fig. 4e, left, significance was determined using one-way analysis of variance (ANOVA), followed by Tukey's multiple comparisons. Significant levels were ranked as follows: $^{*}P < 0.05$, $^{**}P < 0.01$, $^{***}P < 0.001$, NS, not significant. Exact *P* values are given in the numerical source data. The sample number (*n*) indicated in the figure legends shows the number of independent biological samples run in each experiment. Where representative experiments are shown, experiments were repeated at least three times with similar results obtained, unless otherwise noted. All replicate measurements were taken from distinct samples.

Reporting Summary. Further information on research design is available in the Nature Research Reporting Summary linked to this article.

Data availability

All data collected and analysed in this study are available at http://the-rhome.com. The protein interactions from this publication (silver dataset) have been submitted to the IMEx (http://www.imexconsortium.org) consortium through IntAct[86] and assigned the identifier IM-26436. The MS proteomics data have been deposited to the ProteomeXchange Consortium via the PRIDE[87] partner repository with the dataset identifiers PXD010084 and PXD010144. cDNA sequences have been submitted to the European Nucleotide Archive (ENA) (accession numbers LS482294–LS482434). All data can also be found at Biostudies:S-BSST160 (ref. [88]). Source data for Figs. 1, 2, 4, 6–8 and Extended Data Figs. 2, 4 and 5 are available online. All data supporting the findings of this study are also available from the corresponding authors upon reasonable request.

Code availability

The code used for the filtering of the interactome data is available at https://gitlab.ebi.ac.uk/petsalaki/the-rhome. The code for FRET analysis and FA localization analysis is available at https://github.com/paulmarkusmueller/Mueller_et_al_2020 or from the corresponding authors upon request.

References

66. Finn, R. D. et al. The Pfam protein families database: towards a more sustainable future. *Nucleic Acids Res.* **44**, D279–D285 (2016).
67. Eddy, S. R. Accelerated profile HMM searches. *PLoS Comput. Biol.* **7**, e1002195 (2011).
68. Colwill, K. et al. Modification of the Creator recombination system for proteomics applications—improved expression by addition of splice sites. *BMC Biotechnol.* **6**, 13 (2006).
69. Ethier, M., Hou, W., Duewel, H. S. & Figeys, D. The proteomic reactor: a microfluidic device for processing minute amounts of protein prior to mass spectrometry analysis. *J. Proteome Res.* **5**, 2754–2759 (2006).
70. O'Leary, N. A. et al. Reference sequence (RefSeq) database at NCBI: current status, taxonomic expansion, and functional annotation. *Nucleic Acids Res.* **44**, D733–D745 (2016).
71. Liu, G. et al. ProHits: integrated software for mass spectrometry-based interaction proteomics. *Nat. Biotechnol.* **28**, 1015–1017 (2010).
72. Hubner, N. C. et al. Quantitative proteomics combined with BAC TransgeneOmics reveals in vivo protein interactions. *J. Cell Biol.* **189**, 739–754 (2010).
73. Rappsilber, J., Ishihama, Y. & Mann, M. Stop and go extraction tips for matrix-assisted laser desorption/ionization, nanoelectrospray, and LC/MS sample pretreatment in proteomics. *Anal. Chem.* **75**, 663–670 (2003).
74. Cox, J. & Mann, M. MaxQuant enables high peptide identification rates, individualized p.p.b.-range mass accuracies and proteome-wide protein quantification. *Nat. Biotechnol.* **26**, 1367–1372 (2008).
75. Cox, J. et al. Accurate proteome-wide label-free quantification by delayed normalization and maximal peptide ratio extraction, termed MaxLFQ. *Mol. Cell. Proteomics* **13**, 2513–2526 (2014).
76. Schaefer, M. H. et al. HIPPIE: integrating protein interaction networks with experiment based quality scores. *PLoS ONE* **7**, e31826 (2012).
77. Mellacheruvu, D. et al. The CRAPome: a contaminant repository for affinity purification-mass spectrometry data. *Nat. Methods* **10**, 730–736 (2013).
78. Wenger, C. D., Phanstiel, D. H., Lee, M. V., Bailey, D. J. & Coon, J. J. COMPASS: a suite of pre- and post-search proteomics software tools for OMSSA. *Proteomics* **11**, 1064–1074 (2011).
79. Choi, H. et al. SAINT: probabilistic scoring of affinity purification-mass spectrometry data. *Nat. Methods* **8**, 70–73 (2011).
80. Yu, G. & He, Q.-Y. ReactomePA: an R/Bioconductor package for reactome pathway analysis and visualization. *Mol. Biosyst.* **12**, 477–479 (2016).
81. Murtagh, F. & Legendre, P. Ward's hierarchical agglomerative clustering method: which algorithms implement Ward's Criterion? *J. Classification* **31**, 274–295 (2014).
82. Huttlin, E. L. et al. Architecture of the human interactome defines protein communities and disease networks. *Nature* **545**, 505–509 (2017).
83. Hermjakob, H. IntAct: an open source molecular interaction database. *Nucleic Acids Res.* **32**, 452D–455D (2004).
84. Wells, C. D., Gutowski, S., Bollag, G. & Sternweis, P. C. Identification of potential mechanisms for regulation of p115 RhoGEF through analysis of endogenous and mutant forms of the exchange factor. *J. Biol. Chem.* **276**, 28897–28905 (2001).
85. Simpson, J. C., Wellenreuther, R., Poustka, A., Pepperkok, R. & Wiemann, S. Systematic subcellular localization of novel proteins identified by large-scale cDNA sequencing. *EMBO Rep.* **1**, 287–292 (2000).
86. Orchard, S. et al. The MIntAct project—IntAct as a common curation platform for 11 molecular interaction databases. *Nucleic Acids Res.* **42**, D358–D363 (2013).
87. Vizcaíno, J. A. et al. 2016 update of the PRIDE database and its related tools. *Nucleic Acids Res.* **44**, D447–D456 (2016).
88. McEntyre, J., Sarkans, U. & Brazma, A. The BioStudies database. *Mol. Syst. Biol.* **11**, 847 (2015).

Acknowledgements

This work is dedicated to the memory of Tony Pawson, without whom this study would not have been initiated. We thank O. Daumke, R. Hodge, D. Panakova and P. Bieling for critically reading the manuscript, R. D. Fritz and K. Rottner for helpful discussions and F.U.P. Cramer for advice. We thank I. Laue, D. Heidler, H. Naumann and the rest of the Rocks Lab and the MDC Advanced Light Microscopy Facility for technical assistance. This work was supported by the Human Frontier Science Program (LT000759/2008-L) and Helmholtz Young Investigator Program VH-NG-737 (to O.R.), the CIHR Post-doctoral fellowship award (to R.D.B.), the Cancer Research UK (CRUK) Programme Foundation Award (C37275/A20146) and the Stand Up to Cancer campaign for Cancer Research UK (to C. Bakal), and Genome Canada through Ontario Genomics, the Ontario Government (ORF GL2-025) and the Terry Fox Research Institute (to T.P.). Proteomics at the Network Biology Collaborative Centre at the Lunenfeld–Tanenbaum Research Institute was supported by Genome Canada and Ontario Genomics (OGI-139). F.P.R. and E.P. were supported by the Canada Excellence Research Chairs Program, the Krembil Foundation, the Avon Foundation and by the NIH/NHGRI Center of Excellence in Genomic Science program (HG004233).

Author contributions

P.M.M., R.D.B., T.P., E.P. and O.R. conceived the study. Methodologies were developed by the following individuals: P.M.M. (FRET and TIRF screen); P.M.M.,

C. Barth and O.R. (FA segregation); O.R. and C.W. (confocal screen); R.D.B., K.M.A., V.N., M.S.-C., M.T., O. Popp and B.L. (MS); J.R. (PLEKHG4B study and cytochalasin D screen); J.v.U. (FA biosensor analysis); P.M.M., L.E.H., R.D.B., O.R., C. Bakal and E.P. (computational methods); S.Z., L.S., L.B., G.M., T.R., K.F., J.R., P.T. and O.R. (library). E.P., P.M.M., J.R., R.D.B. and O.R. performed the data analyses. E.P., G.G. and P.M.M. developed the software. R.L.E., L.B., M.T.C., C. Barth, R.-W.W., P.P.-V. and P.T. performed other investigations. E.P., P.M.M., R.D.B., J.R. and O.R. curated the data. O. Pertz and K.C. provided reagents. O.R. wrote the paper (with contributions from E.P. and P.M.M). E.P., F.P.R., P.M., A.-C.G. and K.C. were the project administrators, and O.R. supervised the project.

Competing interests

The authors declare no competing interests.

Additional information

Extended data is available for this paper at https://doi.org/10.1038/s41556-020-0488-x.

Supplementary information is available for this paper at https://doi.org/10.1038/s41556-020-0488-x.

Correspondence and requests for materials should be addressed to E.P. or O.R.

Reprints and permissions information is available at www.nature.com/reprints.

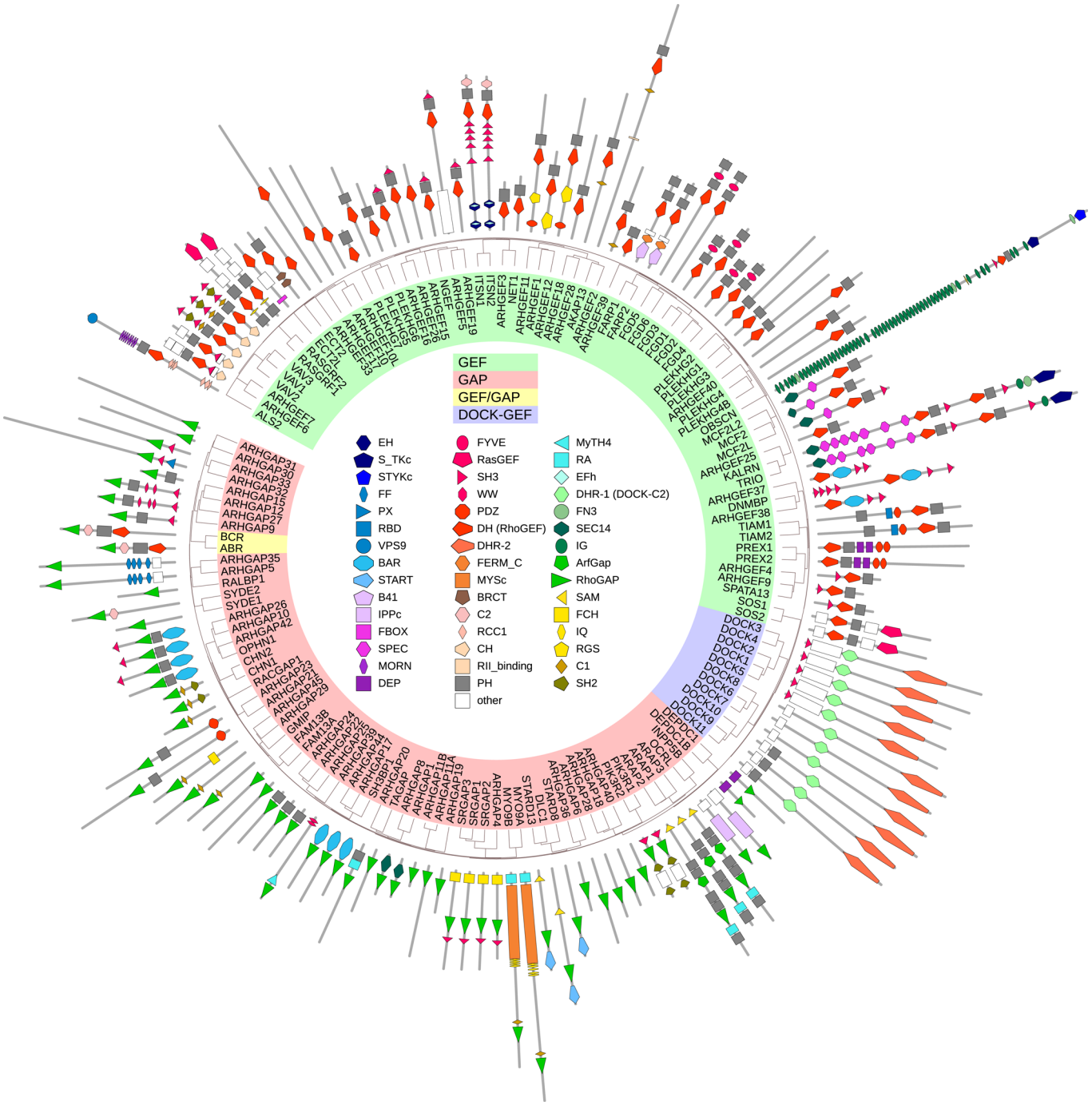

Extended Data Fig. 1 | Domain architecture of the human RhoGEF and RhoGAP proteins. The canonical isoforms of all 145 human RhoGEFs and RhoGAPs containing all distinguishable domains, were collected from UniProt and clustered by multiple sequence alignment using ClustalOmega. The resulting dendrogram and domain structures as predicted by SMART and Pfam (or by Prosite for ARHGEF37 and ARHGEF38) were assembled using iTol. Not all domain families are listed, non-selected ones are indicated as 'other'. IGc2, IG and IG_like were summarized as IG. OBSCN is downscaled by a factor of 0.5. Four cDNAs are not included in our collection: OBSCN (~8000a.a.), as well as ARHGEF33, ARHGEF37 and ARHGEF38 which were originally not predicted as RhoGEFs.

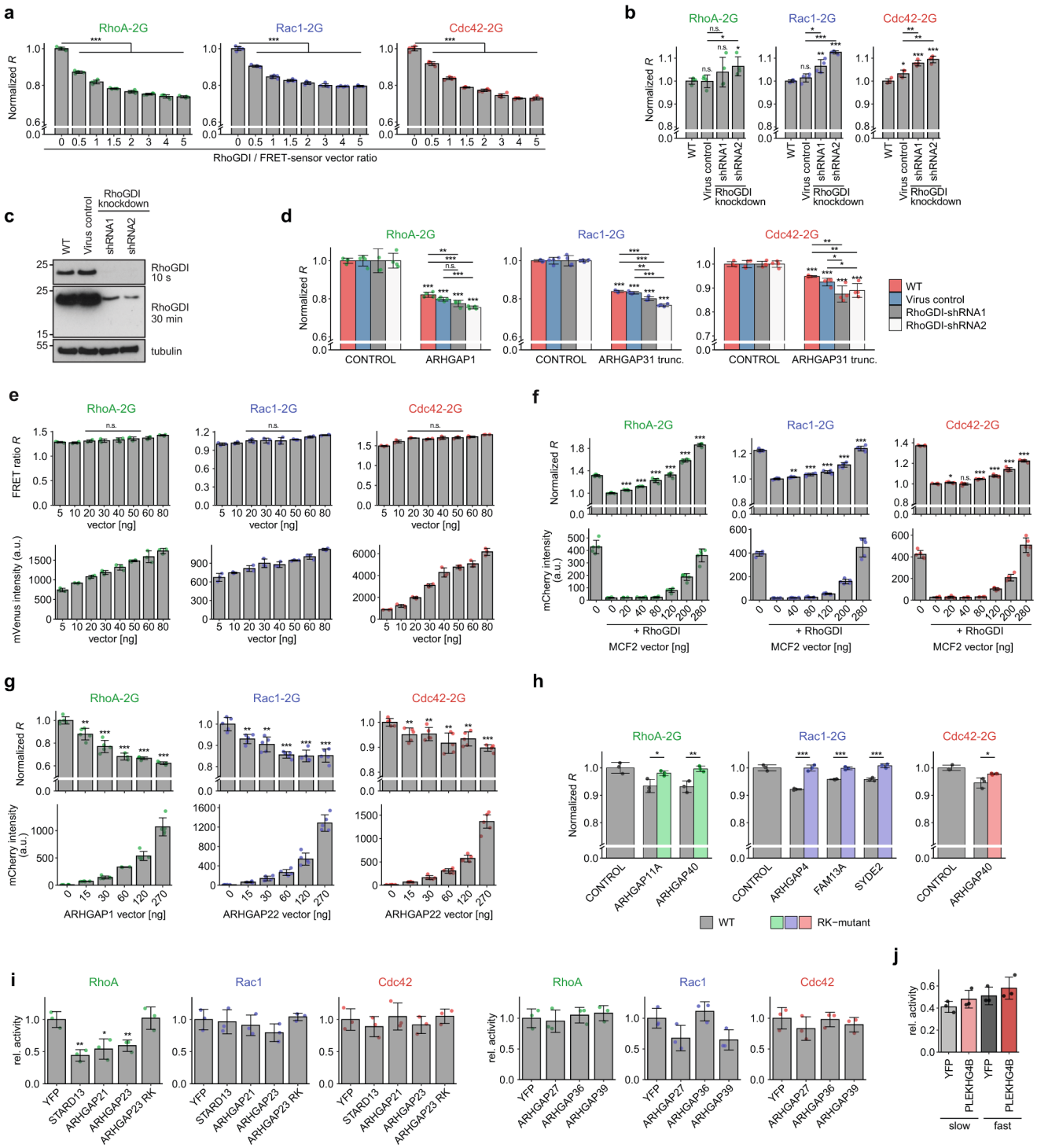

Extended Data Fig. 2 | See next page for caption.

Extended Data Fig. 2 | Establishment of the FRET-based RhoGEF/RhoGAP activity screen. a, RhoGDI restores basal activity levels of overexpressed Rho sensors, facilitating RhoGEF assays. Data represents mean ± SD normalized to RhoGDI/sensor vector ratio 0, n=5 FOV of one sample, experiment repeated once with similar results. **b**, RhoGDI depletion increases the basal activity of the Rho biosensors, facilitating RhoGAP assays. Data represents mean ± SD normalized to WT, n=4 independent experiments. **c**, Western blot showing shRNA-mediated RhoGDI-knockdown in cell lines used in (b) and (d) compared to virus and non-infected (WT) controls. Representative example out of three experiments with similar results. **d**, Biosensor response to RhoGAPs is more pronounced in RhoGDI-depleted cells. Cell lines as in (c) were transfected with Rho sensors and RhoGAPs or mCherry (control). Data represents mean ± SD normalized to control of each cell line, n=4 independent experiments. **e**, FRET ratio is stable across a wide range of sensor expression levels. Cells were transfected with indicated amounts of biosensor vector. mVenus intensity represents relative sensor expression levels. Data represents mean ± SD, n=3 independent experiments. *p*-values were calculated by unpaired two-sided Student's t-tests between each of the samples under the line. **f** and **g**, Minimal RhoGEF or RhoGAP levels are sufficient to alter the Rho GTPase activity state. HEK293T (f) or RhoGDI-shRNA2 HEK293T (g) cells were cotransfected with Rho sensors and increasing amounts of mCherry-tagged MCF2 (together with 80 ng RhoGDI where indicated, or 80 ng mCherry) or increasing amounts of mCherry-ARHGAP1 or mCherry-ARHGAP22, respectively. mCherry intensities represent relative RhoGEF or RhoGAP expression levels. Data represents mean ± SD normalized to the 0 ng MCF2+RhoGDI sample or normalized to the 0 ng RhoGAP sample, respectively, n=5 FOV of one sample, experiment repeated once with similar results. **h**, The FRET assay detects only catalytically active RhoGAPs (WT) but not GAP-deficient RK-mutants (ARHGAP4-R543K, ARHGAP11A-R87K, ARHGAP40-R311K, FAM13A-R81K, SYDE2-R854K). Data represents mean ± SD normalized to WT control (mCherry), n=3 independent experiments. **i**, G-LISA pulldown assay data confirming the substrate specificities found in Fig. 1 for a subset of regulators. RK: ARHGAP23-R986K in lysates. Data represents mean ± SD normalized to YFP, n=3 independent experiments. **j**, Error-propagation in pulldown assays due to fast GTP hydrolysis. Lysates of transfected HEK293T cells were either processed as fast as possible or with the maximum allowed time according to manual, before processing by Cdc42 GLISA assay. Data represents mean ± SD normalized to YFP, n=3 independent experiments. (**a**-**h**) All *p*-values were calculated by unpaired two-sided Student's t-test against WT, CONTROL, YFP or 0 ng vector transfected or as indicated by lines and ranked as ***p<0.001, **p<0.01, *p<0.05, n.s.=not significant. Source data including *p*-values is provided in Source Data Extended Data Fig. 2.

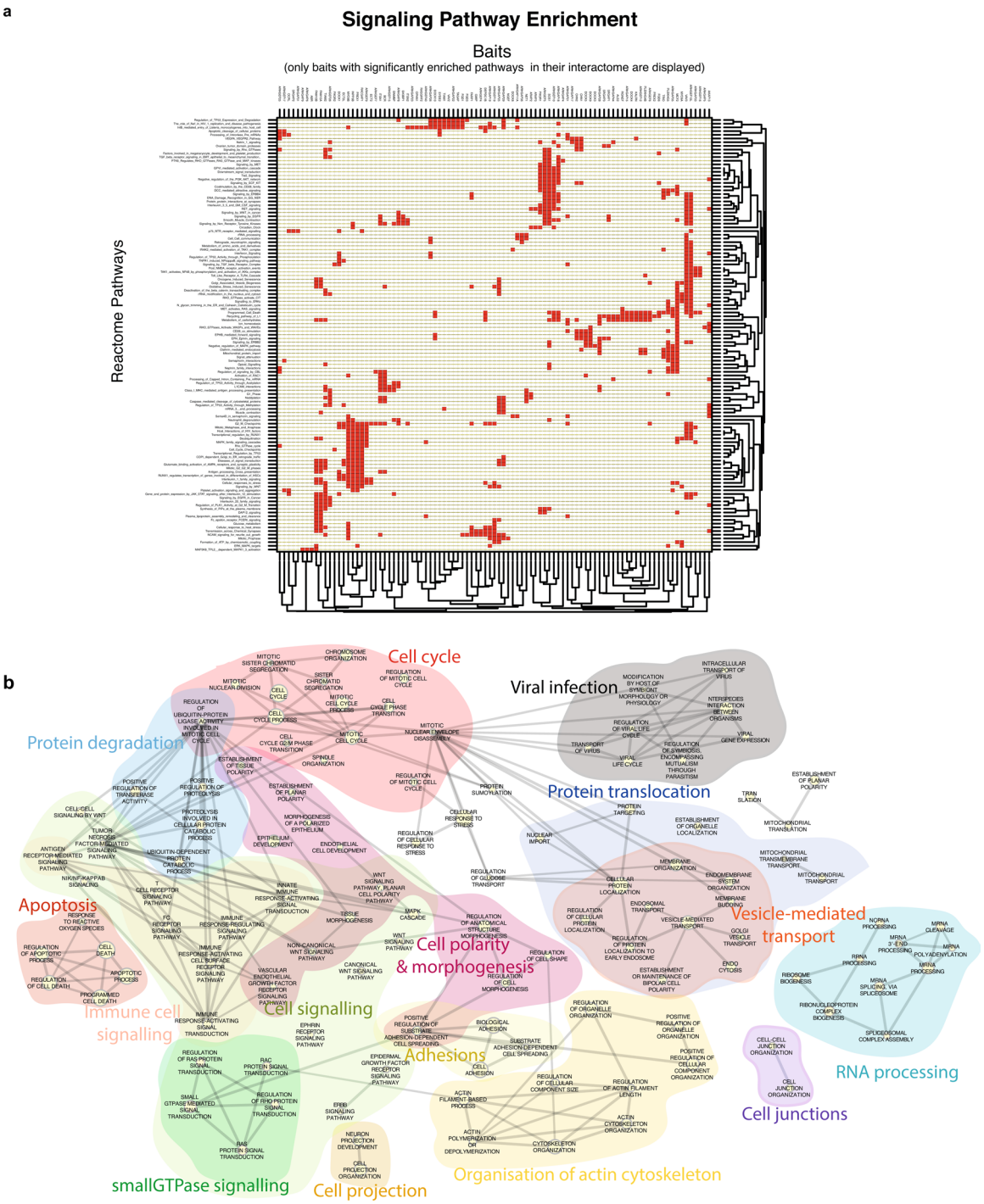

Extended Data Fig. 3 | Reactome pathways enrichment analysis and GO Terms enrichment analysis. a, Pathway enrichment analysis was performed using the ReactomePA function from Bioconductor. Clustering was done using the hclust function in R. **b**, GO Terms enrichment analysis was performed using the Funcassociate 3.0 web server (http://llama.mshri.on.ca/funcassociate/). Edges between GO terms were calculated using vectors of the genes included in the term and our set and calculating the Jaccard index. Highly redundant nodes were reduced manually to the most informative one for improved visualization (e.g. among the nodes: 'Cell process', 'regulation of cell process', 'positive regulation of cell process', only 'Cell process' is kept). Results were visualized using Cytoscape. Our 1292 interactions were used for this enrichment and as background the entire human proteome.

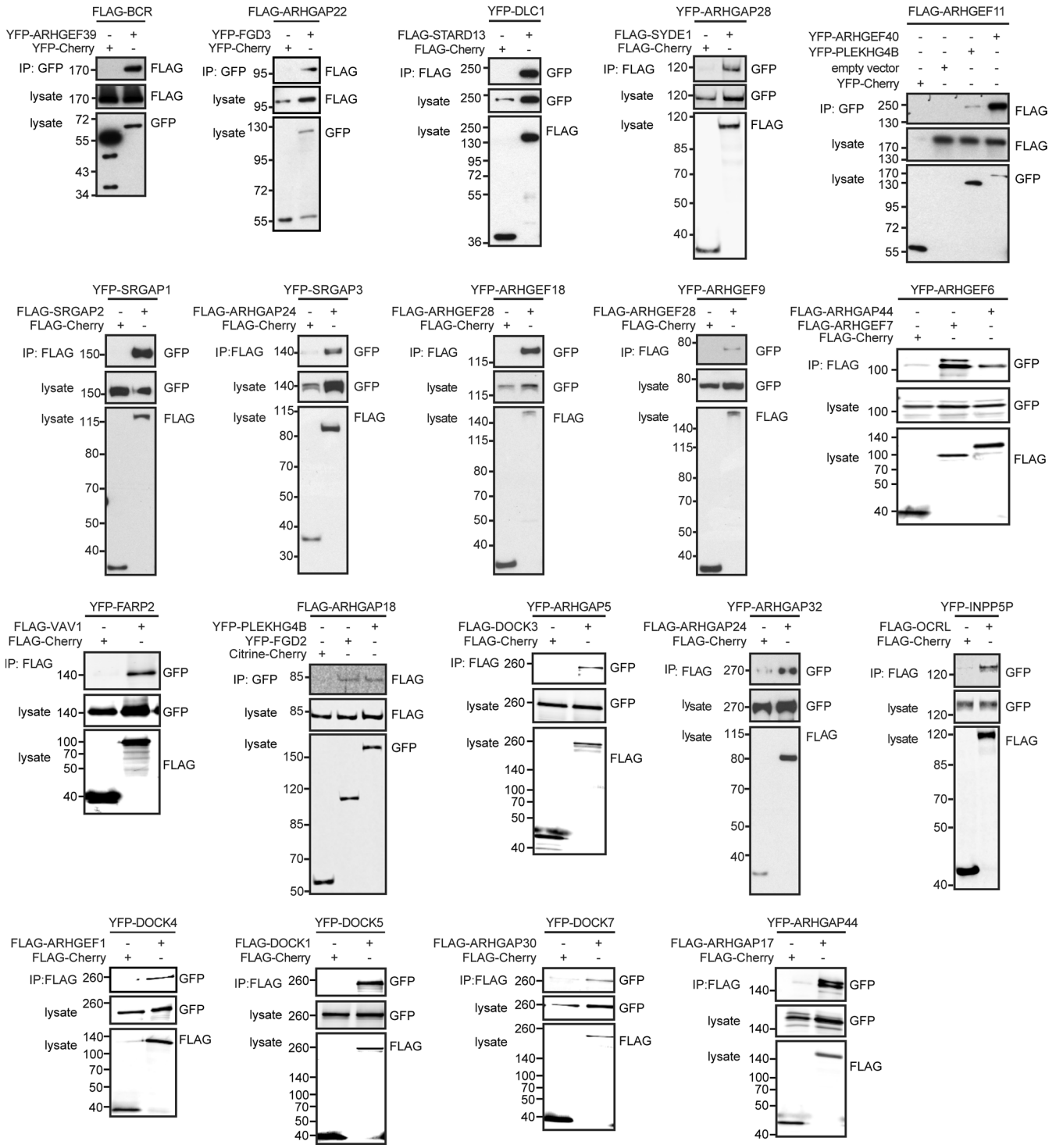

Extended Data Fig. 4 | Validation of interactions between RhoGEFs and RhoGAPs identified by mass spectrometry. To assess the quality of the network dataset, lysates of HEK293T cells transfected with the indicated YFP- and FLAG-tagged regulators or controls were immunoprecipitated (IP) as indicated using either a FLAG or GFP antibody and subsequently immunoblotted using a corresponding GFP or FLAG antibody. Protein bands were detected either by chemiluminescence or using a gel imaging system. 22 out of 26 RhoGEF/RhoGAP pairs tested were successfully validated in two independent repeats. See Source Data_Extended Data Fig. 4 for unprocessed blots.

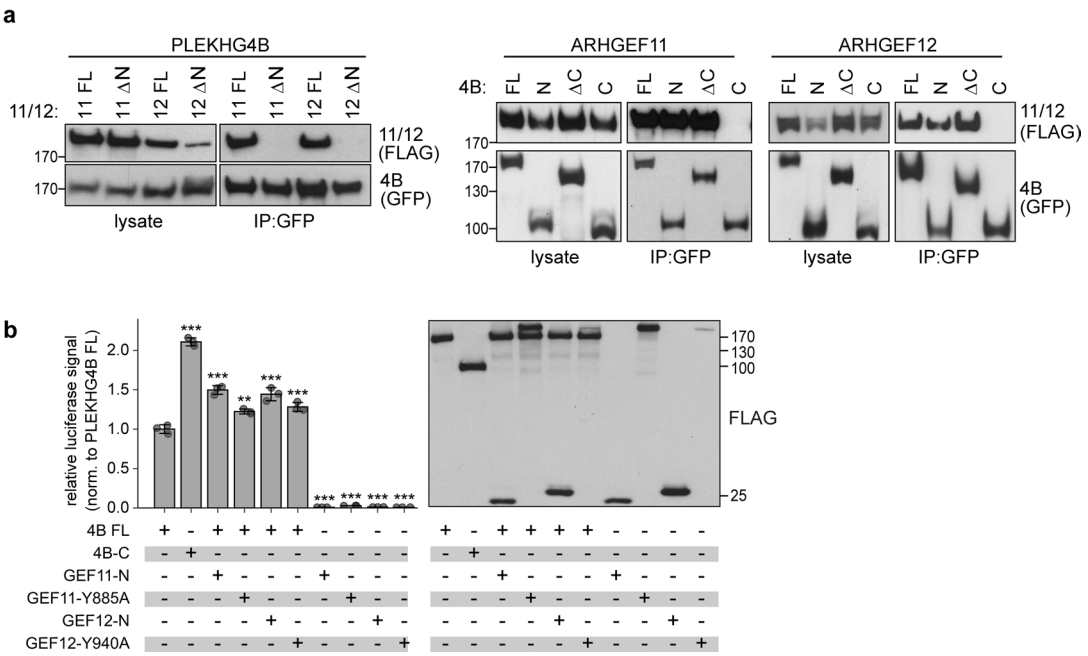

Extended Data Fig. 5 | Characterization of the PLEKHG4B/ARHGEF11/ARHGEF12 multi-RhoGEF complex. a, PLEKHG4B, ARHGEF11 and ARHGEF12 interact via their N-termini. Immunoprecipitation assays (IP) performed in HEK293T cells expressing YFP-PLEKHG4B together with the indicated full-length or truncated FLAG-ARHGEF11 or FLAG-ARHGEF12 constructs (left panel) or FLAG-ARHGEF11 or FLAG-ARHGEF12 together with the indicated full-length or truncated YFP-PLEKHG4B constructs (right panel). Data are representative of 2 independent experiments. **b**, PLEKHG4B autoinhibition is released by ARHGEF11 and ARHGEF12. Anti-FLAG Western Blot corresponding to the SRE-luciferase reporter activation data presented in Fig. 4e, left panel, showing the expression of the transfected constructs. Mean ± SD (n=3 independent samples of one experiment, representative out of three experiments with similar results). Significance was determined using One-way ANOVA, followed by Tukey's multiple comparisons. Significance was ranked as *** p<0.001. Numerical source data including *p*-values is available online. See Source Data_Extended Data Fig. 5 for unprocessed blots.

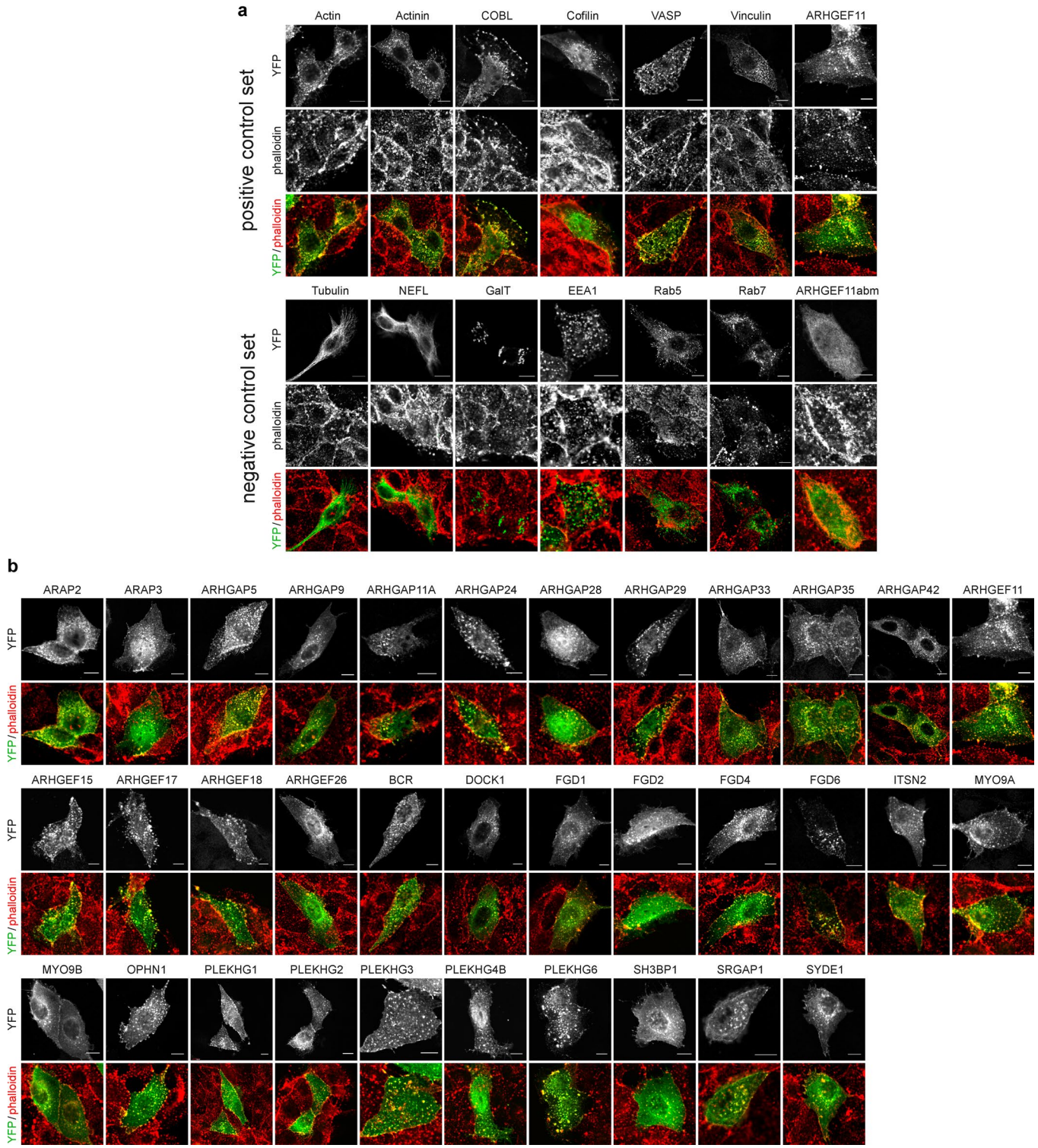

Extended Data Fig. 6 | Cytochalasin D screen reveals actin-associated RhoGEFs and RhoGAPs. Confocal images of MDCK cells transiently transfected with YFP fusion constructs of the indicated **a**, positive (upper panel) or negative (lower panel) control proteins, or **b**, YFP-tagged RhoGEFs and RhoGAPs. Cells were treated for 30 min with cytochalasin D, fixed and stained for actin with phalloidin. YFP signals were enhanced by anti-GFP immunofluorescence (green: YFP, red: actin in merged images). All 34 actin-associated regulators are displayed. Representative images of two independent experiments (with five images obtained for each experiment) with similar results are shown. Scale bars: 10 µm. The assay not only reliably identified all 12 regulators that we found to colocalize with actin in the primary confocal microscopy screen but also a set of known actin-associated proteins. No coaggregation was observed for negative control proteins known either to be cytosolic or to localize to other compartments. In addition, ARHGEF11, a RhoGEF that associates with actin filaments but is not detectable through microscopy on this structure, was found to coaggregate with actin, while a mutant deficient in actin binding[64] (ARHGEF11abm) did not.

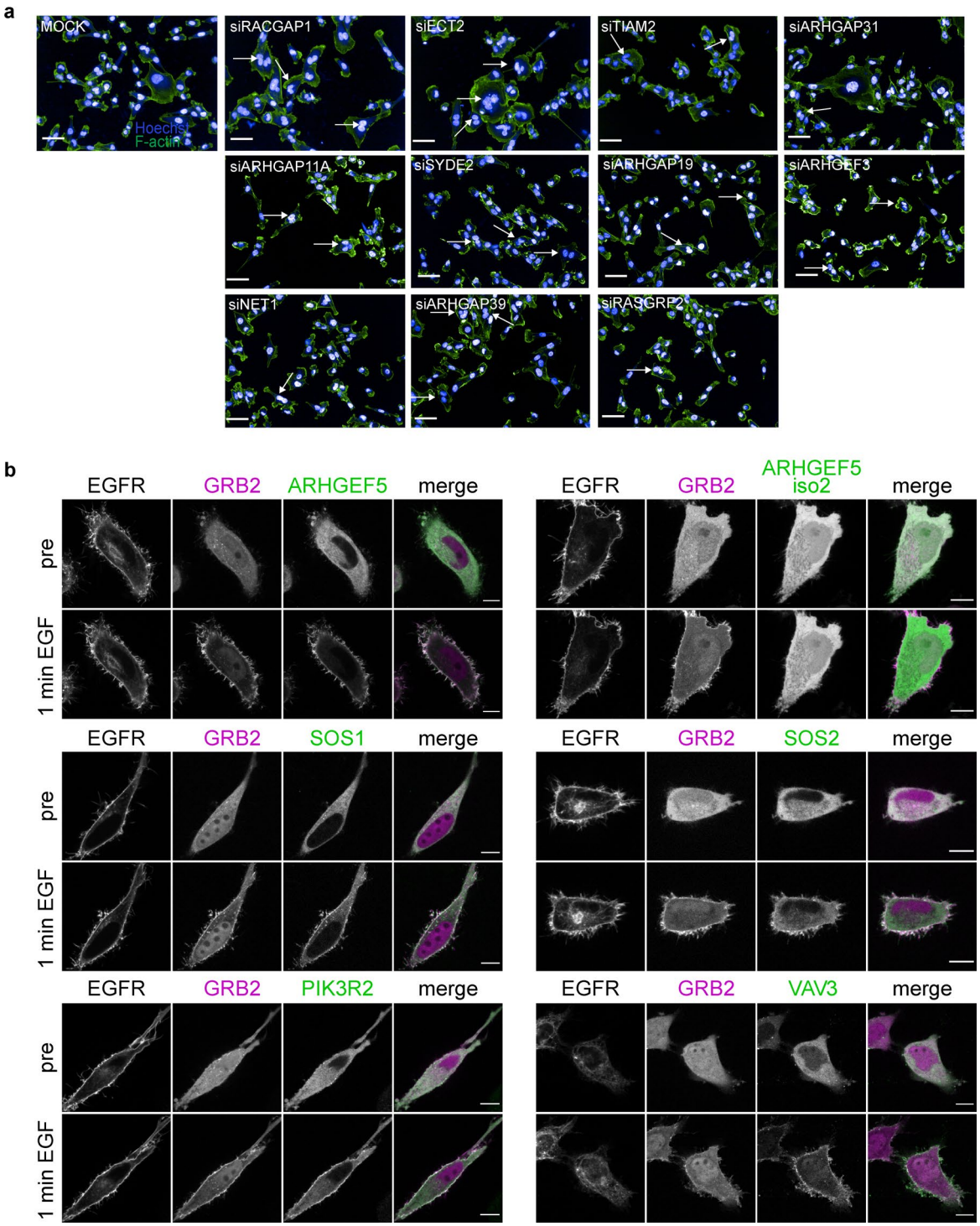

Extended Data Fig. 7 | RhoGEFs and RhoGAPs provide positional information to Rho signalling regulation. a, Images from genome-wide siRNA knockdown screen in MDA-MB-231 cells, related to Fig. 6a. Shown are representative examples of abnormal nuclei in cells treated with siRNA against the indicated eleven RhoGEFs/RhoGAPs identified in this study to localize in the nucleus. Experiment was done in quadruplicates. Scale bars: 50 µm. **b**, Live confocal micrographs of HeLa cells coexpressing EGFR-CFP, mRFP-GRB2 and the indicated YFP-tagged RhoGEFs/RhoGAPs before and 1 min after EGF stimulation (100 ng/ml), related to Fig. 6b. 25 candidate GRB2-interactors were tested: eight regulators identified in our interactome analysis (Supplementary Table 3) and additional proteins listed in the BioGRID database (https://thebiogrid.org/). HeLa cells were chosen because of their robust responsiveness to growth factor stimulation, resulting in an almost complete GRB2 recruitment to the plasma membrane. Only direct interactors of GRB2 co-translocate to the plasma membrane to the same extent. Note, that ARHGEF5 isoform 2, lacking a large N-terminal portion, does not bind GRB2 and remains cytosolic. Representative examples of three independent stimulation experiments with similar results are shown. Scale bars: 10 µm.

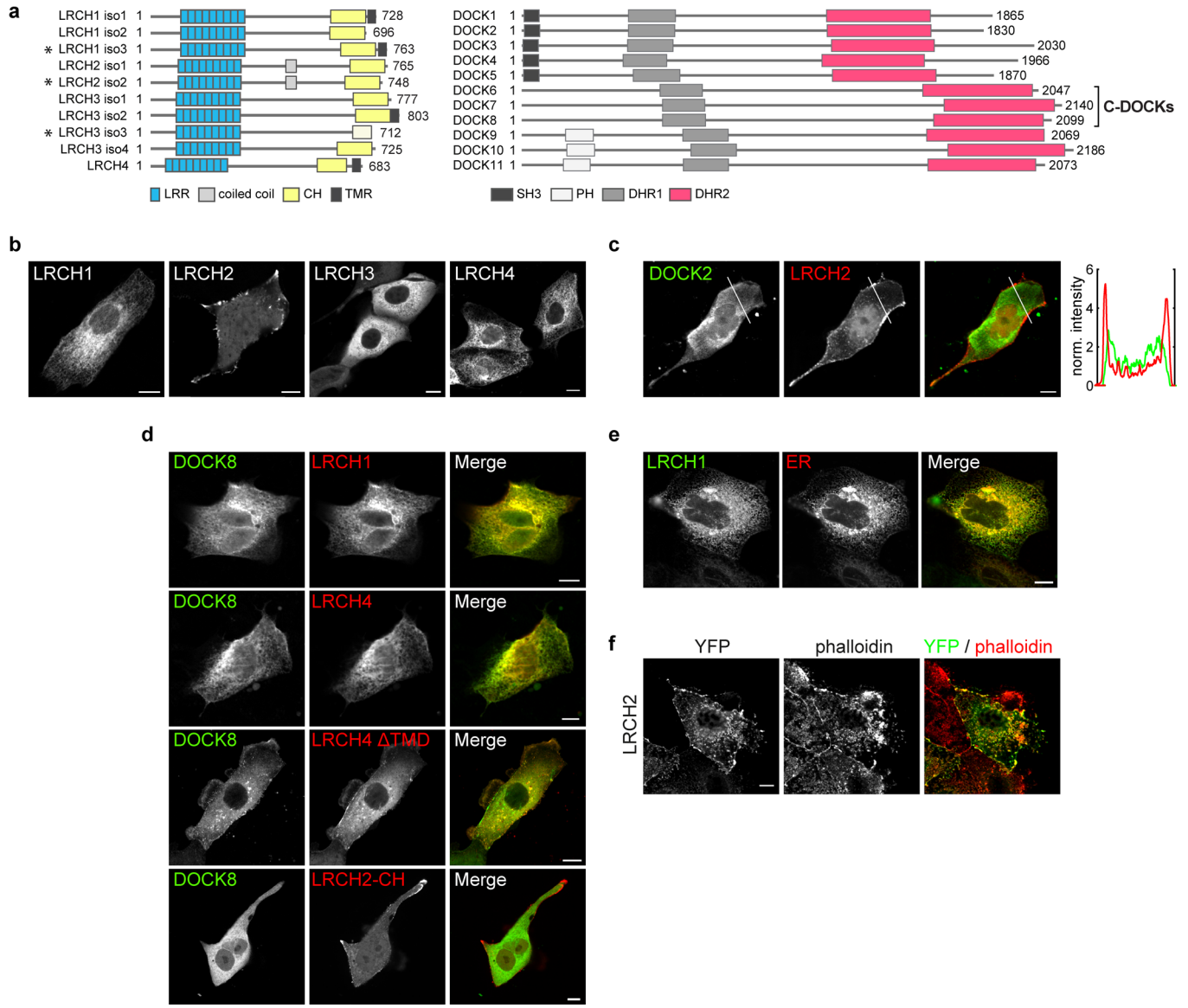

Extended Data Fig. 8 | C-DOCK subfamily RhoGEFs interact with LRCH family proteins. a, Domain architecture of all human LRCH family proteins and their isoforms and all eleven DOCK family proteins. Asterisks (*) mark LRCH protein isoforms used in this study. LRR: Leucin rich repeats; CH: Calponin homology; TMR: transmembrane region; SH3: Src homology 3; PH: Pleckstrin homology; DHR: DOCK homology region. **b**, Live confocal micrographs of MDCK cells expressing all four LRCH proteins (YFP). Note the compromised CH domain in LRCH3 isoform 3 used in this study which may account for its cytosolic localization. **c**, The A-DOCK family protein DOCK2 (YFP) is not recruited by LRCH2 (CFP) to the periphery of MDCK cells. Live confocal micrographs related to Fig. 6d. **d**, Live confocal micrographs of MDCK cells coexpressing CFP-DOCK8 and the indicated LRCH proteins and fragments thereof, showing the recruitment of DOCK8 to the endoplasmic reticulum by LRCH1 and LRCH4, or to the cell periphery by LRCH4-ΔTMR. LRCH2-CH, lacking the Leucine rich repeats, cannot recruit DOCK8 to the cell periphery. **e**, Live confocal micrographs of MDCK cells coexpressing CFP-LRCH1 and the ER marker PTP1B-YFP, revealing their colocalization (related to Fig. 6h). **f**, Cytochalasin D experiment related to Fig. 6i, revealing actin association of full-length LRCH2. Scale bars: 10 μm. All confocal images are representative of three independent experiments with similar results.

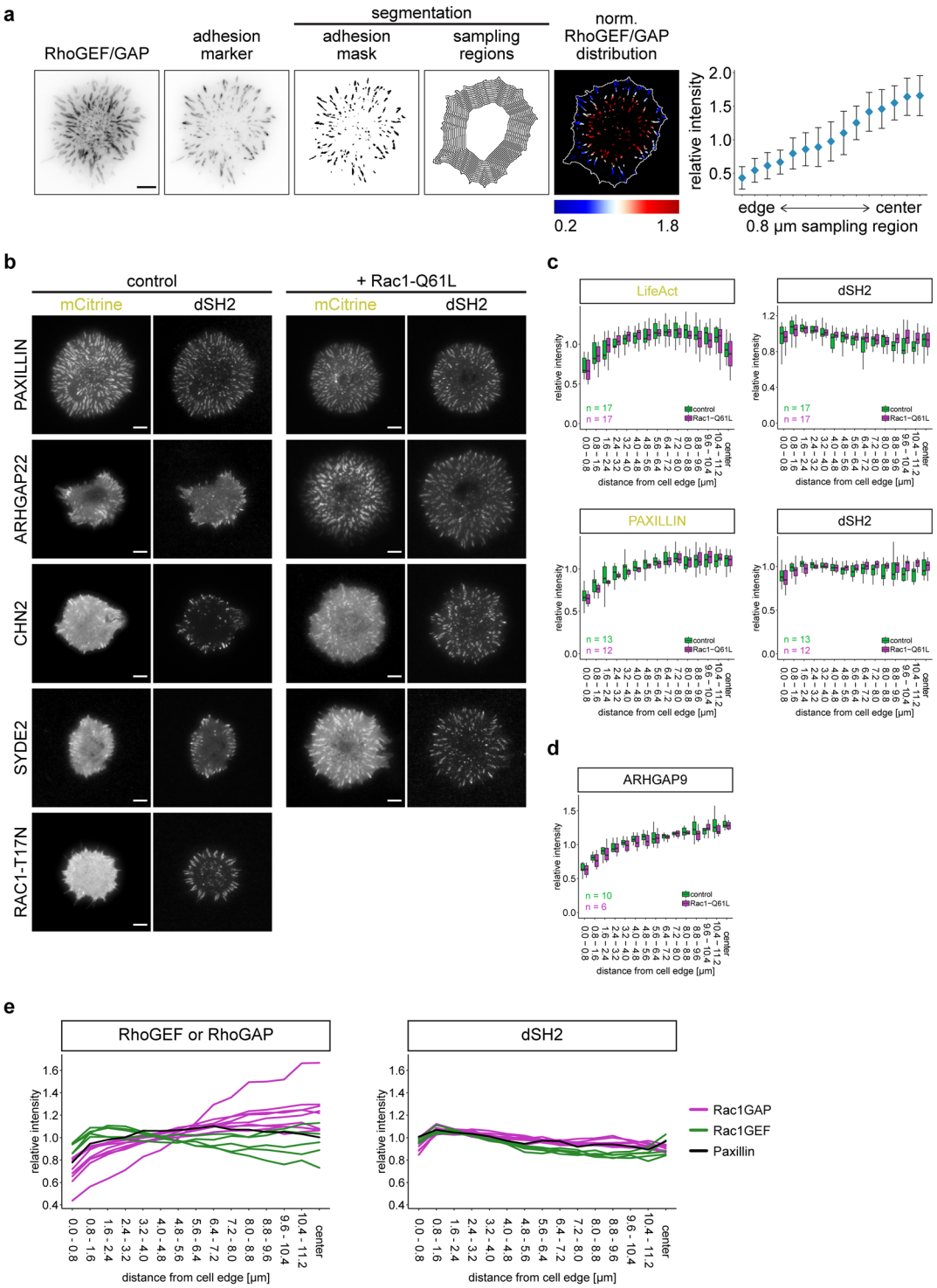

Extended Data Fig. 9 | See next page for caption.

Extended Data Fig. 9 | Spatial segregation of RAC1-specific GEFs and GAPs on integrin adhesions in spreading cells. a, Quantification of RhoGEF/RhoGAP distribution on integrin adhesions. REF52 fibroblasts were transfected with YFP-tagged regulators and the adhesion marker mScarlet-dSH2, together with the plasma membrane marker miRFP-KRas-HVR, or with iRFP-RAC1-Q61L for RAC1-specific GAPs, to balance the GAP phenotype (see (b-e)). Normalized intensity at adhesion complexes is false colour-coded as indicated. Graph shows normalized mean intensity over all pixels of each sampling region ± SD (n=number of pixels in each sampling region) of the example cell on the left. See Methods for details. **b**, The spreading phenotype induced by RAC1-specific GAPs can be re-balanced by coexpression of low levels of constitutively active RAC1 (RAC1-Q61L). Dominant negative RAC1 (RAC1-T17N) causes a spreading phenotype similar to RAC1-specific GAPs. REF52 cells were transfected with YFP-tagged Paxillin control, the exemplary RAC1-specific GAPs ARHGAP22, CHN2 or SYDE2, or dominant negative RAC1 (RAC1-T17N)), together with mScarlet-dSH2 and miRFP-KRas-HVR (control, left panel) or iRFP-RAC1-Q61L (right panel). Experiment was repeated three times with similar results. **c**, Expression of RAC1-Q61L does not alter the relative distribution of actin, paxillin and phospho-tyrosine on integrin adhesions in isotropically spreading cells. REF52 cells were transfected with mEGFP-LifeAct or mEGFP-Paxillin, together with mScarlet-dSH2 (phospho-tyrosine adhesion marker) and miRFP-KRas-HVR (control) or iRFP-RAC1-Q61L. **d**, Expression of RAC1-Q61L does not alter the relative distribution of ARHGAP9 in isotropically spreading cells. ARHGAP9 is a RAC1-specific GAP showing only a mild spreading phenotype. REF52 cells in (b), (c), and (d) were treated as in (a). n in (c) and (d) is given as number of analyzed cells inside the graph. **e**, Expression of RAC1-GEFs, or of RAC1-GAPs together with RAC1-Q61L, does not alter the relative distribution of dSH2 on integrin adhesions in isotropically spreading cells. Left panel: Quantification of GEF/GAP distributions as shown in Fig. 7e, right panel: corresponding distributions of dSH2. Means of n=9–23 cells from one experiment are shown (for details on n see Supplementary Information Fig. 3). All scale bars: 10 μm. Boxplot centre lines in (c) and (d) represent the median values, box limits the 25th and 75th percentiles; whiskers extend 1.5 times the interquartile range from the 25th and 75th percentiles.

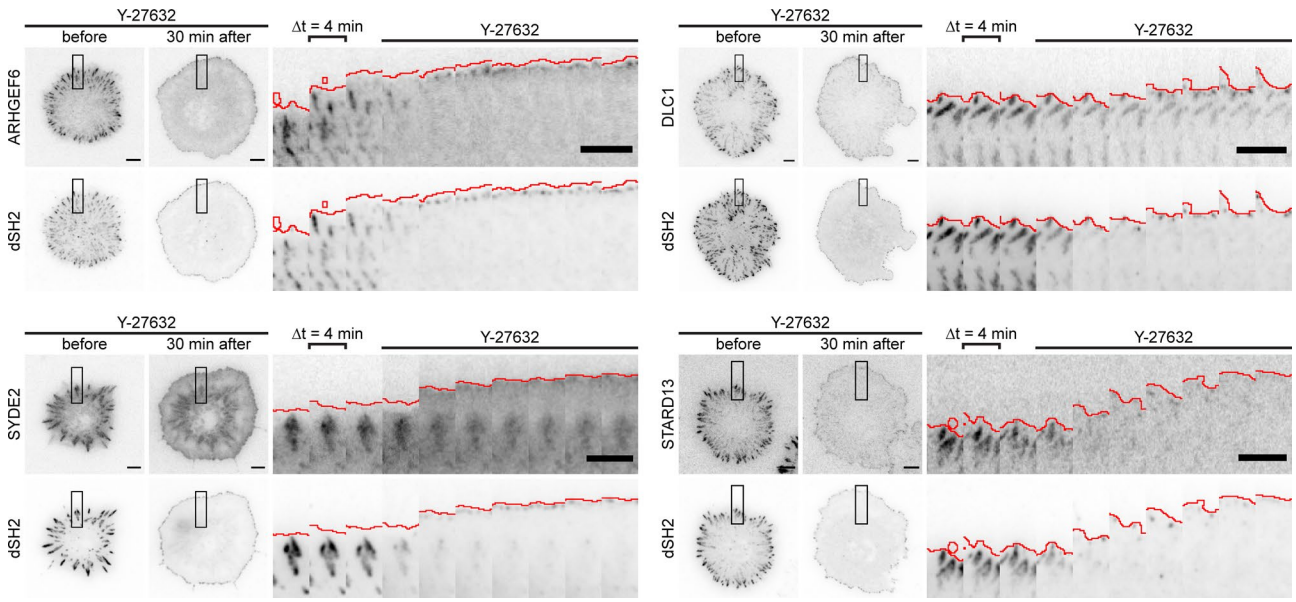

Extended Data Fig. 10 | RhoGEF/RhoGAP re-distribution on focal adhesions in isotropically spreading cells upon Y-27632 addition. Timelapse images showing RhoGEF/RhoGAP re-distribution on adhesions in isotropically spreading cells upon Y-27632 addition (corresponding to Supplementary Videos 3–6). REF52 cells were treated as in Fig. 7d. Left panel: representative timepoints before and 30 min after addition of inhibitor. Right panel: kymographs of boxed regions with the cell edge marked in red. Note, that the RAC1-specific GEF ARHGEF6, as well as the RHOA-specific GAPs DLC1 and STARD13, localize to early nascent adhesions after Y-27632 treatment (as indicated by dSH2 close to the cell edge), whilst the RAC1-specific GAP SYDE2 does not. Data shown represent four, five, three and four independent experiments for ARHGEF6, DLC1, SYDE2 and STARD13, respectively. All scale bars: 10 μm.

nature research

Corresponding author(s): Dr Oliver Rocks and Dr Evangelia Petsalaki

Last updated by author(s): Jan 22, 2020

Reporting Summary

Nature Research wishes to improve the reproducibility of the work that we publish. This form provides structure for consistency and transparency in reporting. For further information on Nature Research policies, see Authors & Referees and the Editorial Policy Checklist.

Statistics

For all statistical analyses, confirm that the following items are present in the figure legend, table legend, main text, or Methods section.

n/a	Confirmed
☐	☒ The exact sample size (*n*) for each experimental group/condition, given as a discrete number and unit of measurement
☐	☒ A statement on whether measurements were taken from distinct samples or whether the same sample was measured repeatedly
☐	☒ The statistical test(s) used AND whether they are one- or two-sided *Only common tests should be described solely by name; describe more complex techniques in the Methods section.*
☒	☐ A description of all covariates tested
☐	☒ A description of any assumptions or corrections, such as tests of normality and adjustment for multiple comparisons
☐	☒ A full description of the statistical parameters including central tendency (e.g. means) or other basic estimates (e.g. regression coefficient) AND variation (e.g. standard deviation) or associated estimates of uncertainty (e.g. confidence intervals)
☒	☐ For null hypothesis testing, the test statistic (e.g. *F*, *t*, *r*) with confidence intervals, effect sizes, degrees of freedom and *P* value noted *Give P values as exact values whenever suitable.*
☒	☐ For Bayesian analysis, information on the choice of priors and Markov chain Monte Carlo settings
☒	☐ For hierarchical and complex designs, identification of the appropriate level for tests and full reporting of outcomes
☐	☒ Estimates of effect sizes (e.g. Cohen's *d*, Pearson's *r*), indicating how they were calculated

Our web collection on statistics for biologists contains articles on many of the points above.

Software and code

Policy information about availability of computer code

Data collection	Columbus image analysis software: Perkin Elmer 2.6.0, Mascotv2.3, TPP, ProHits, MaxQuant version 1.5.2.8, MaxLFQ, ODYSSEY LI-COR
Data analysis	Funcassociate 3.0 & DAVID 6.8, Cluster 3.0, HMMER 3.1b2, Cytoscape 3.4,JMP Pro 11.0.0, TMHNN v2.0, RefSeqV42 & V57, uniprot release-2015_09, Fiji, ClustalOmega1.2.1, iTOL, CLC sequence viewer, https://gitlab.ebi.ac.uk/petsalaki/the-rhome, Rv3.0, Morpheus

For manuscripts utilizing custom algorithms or software that are central to the research but not yet described in published literature, software must be made available to editors/reviewers. We strongly encourage code deposition in a community repository (e.g. GitHub). See the Nature Research guidelines for submitting code & software for further information.

Data

Policy information about availability of data

All manuscripts must include a data availability statement. This statement should provide the following information, where applicable:

- Accession codes, unique identifiers, or web links for publicly available datasets
- A list of figures that have associated raw data
- A description of any restrictions on data availability

All data collected and analyzed in this study, extended versions of the Supplementary tables, along with additional links to existing databases is available here http://the-rhome.com. The protein interactions from this publication (silver dataset) have been submitted to the IMEx (http://www.imexconsortium.org) consortium through IntAct77 and assigned the identifier IM-26436. The mass spectrometry proteomics data from the Q Exactive HF-X run have been deposited to the ProteomeXchange Consortium via the PRIDE54 partner repository with the dataset identifier PXD010084. The rest of the mass spectrometry proteomics data have been deposited under the dataset identifier PXD010144. cDNA sequences have been submitted to the ENA database and assigned the accession numbers LS482294-LS482434. Detailed information, including sequences of the inserts in our cDNA library is provided in table S1. All data, figures and files can also be found in Biostudies:S-BSST16011 https://www.ebi.ac.uk/biostudies/studies/S-BSST16078. The code used for the filtering of the interactome data is available here: https://gitlabci.ebi.ac.uk/petsalaki/the-rhome. The code for FRET analysis and focal adhesion localization analysis is available here: https://github.com/paulmarkusmueller/Mueller_et_al_2020 or from the corresponding authors upon request..

Field-specific reporting

Please select the one below that is the best fit for your research. If you are not sure, read the appropriate sections before making your selection.

☒ Life sciences ☐ Behavioural & social sciences ☐ Ecological, evolutionary & environmental sciences

For a reference copy of the document with all sections, see nature.com/documents/nr-reporting-summary-flat.pdf

Life sciences study design

All studies must disclose on these points even when the disclosure is negative.

Sample size	As our study does not seek to make associations of one feature with another, there was no requirement for a specific sample size to give us statistical power. For each RhoGEF/RhoGAP, we performed at minimum 2 replicates of the pull downs for mass spectrometry, as is standard practice in the field. The RhoGEF/RhoGAP substrate specificity screen was performed at 3 independent replicates. Further information on sample size can be found in the figure legends and the methods section.
Data exclusions	AP/MS samples were excluded if the bait was not detected in the peptides identified, as this indicates that the experiment was unsuccessful. These criteria were pre-established.
Replication	Pull down samples were performed at least twice with different tags to ensure that the prey identified are not artifacts of the tag used on the bait. Further information on replication can be found in the figure legends and the methods section. All attempts at replication were successful.
Randomization	No experimental groups were defined in this study as it is a systematic study of mammalian RhoGEFs/GAPs and therefore no randomization was required.
Blinding	No experimental groups were defined in this study as it is a systematic study of mammalian RhoGEFs/GAPs and therefore no blinding was required.

Reporting for specific materials, systems and methods

We require information from authors about some types of materials, experimental systems and methods used in many studies. Here, indicate whether each material, system or method listed is relevant to your study. If you are not sure if a list item applies to your research, read the appropriate section before selecting a response.

Materials & experimental systems

n/a	Involved in the study
☐	☒ Antibodies
☐	☒ Eukaryotic cell lines
☒	☐ Palaeontology
☒	☐ Animals and other organisms
☒	☐ Human research participants
☒	☐ Clinical data

Methods

n/a	Involved in the study
☒	☐ ChIP-seq
☒	☐ Flow cytometry
☒	☐ MRI-based neuroimaging

Antibodies

Antibodies used	Rabbit anti-GFP (WB), abcam, ab290, 1:10000 Rabbit anti-GFP (IF), Molecular Probes, A11122, 1:5000 Chicken anti-GFP (IF), abcam, ab13970, 1:1000 Mouse anti-FLAG-M2 (WB), Sigma, F3165, 1:5000 Rabbit anti-RhoGDI (WB), Santa Cruz, sc360, 1:2000 Mouse anti-alpha-Tubulin (WB), Sigma, T6199 (cloneDM1A), 1:10000 Mouse anti-alpha-Tubulin (IF), Thermo Fisher Scientific, A11126, 1:1000 Mouse anti-Cherry (WB), abcam, ab125096, 1:2000 F(ab')2-Goat anti-Mouse IgG (H+L) Secondary Antibody, Alexa Fluor 647, Molecular Probes, A216237, 1:1000 Goat anti-Rabbit IgG (H+L) Secondary Antibody, Alexa Fluor 488, Molecular Probes, A11008, 1:1000 Goat anti-Chicken IgY (H+L) Secondary Antibody, Alexa Fluor 488, Molecular Probes, A11039, 1:1000 Goat anti-Mouse IgG (H L)-HRP Conjugate, Bio-Rad, 1706516, 1:10000 Goat anti-Rabbit IgG (H L)-HRP Conjugate, Bio-Rad, 1706515, 1:10000 IRDye 800CW Donkey anti-Mouse IgG (H+L), Li-COR, 926-32212, 1:10000
Validation	All antibodies used in this study are commercially obtained and were validated by the commercial suppliers (see specific websites for full information).

Eukaryotic cell lines

Policy information about cell lines

Cell line source(s)	HEK293T were obtained from ATCC (#CRL-3216), MDCK II from Prof. Philippe Bastiaens (MPI Dortmund), COS-7 from ATCC (#CRL-1651) and REF52 cells from Prof. Klemens Rottner (HZI Braunschweig). COS-7-Cherry-Paxillin and HEK293T-RhoGDI-shRNA#1 and -shRNA#2 were generated in our laboratory.
Authentication	Cell lines were not independently authenticated.
Mycoplasma contamination	Cell lines were routinely tested for mycoplasma and were certified to be negative.
Commonly misidentified lines (See ICLAC register)	No commonly misidentified cell lines were used in this study.